Future global population exposure to record-breaking climate extremes

Bohao Li[1], Kai Liu[1], Ming Wang[1], Qianzhi Wang[1], Qian He[1], and Chenxia Li[2]

[1]Beijing Normal University
[2]Capital Normal University

May 13, 2023

Abstract

The increase in record-breaking extreme events caused by climate change poses a threat to human health and well-being; understanding the future impacts of such events on global populations can provide decision-making support for policies aiming to mitigate climate change. Here, we investigated the population exposure to eight climate extreme indices and drivers of exposure trajectories based on NASA Earth Exchange Global Daily Downscaled Projections Coupled Model Intercomparison Project 6 (CMIP6) and population projection data under four shared socioeconomic pathway (SSP) scenarios at a spatial resolution of 0.25°×0.25°. The results show that by the mid-21st century, most regions around the world, especially Africa and South America, will continue to experience record-breaking temperatures and compound drought and heatwaves (CDHWs). Regarding population exposure, under the worst-case scenario of SSP3-7.0 in the late 21st century, the mean value of the multimodel median expected annual exposure (EAE) of all extreme temperature indices and CDHW reaches 8.79 billion persons per year; population exposure hotspots will be concentrated in Central Africa, South Asia, Southeast Asia, and East Asia, mostly in developing countries, where 62.77%-87.42% of the EAE is found. The drivers of exposure trajectories are spatially heterogeneous; the increase in record-breaking probability contributes more than population growth to EAE growth in most regions of the world except Central Asia, the Middle East, and most of Africa. These findings highlight the necessity of using various climate extreme indices to reveal spatiotemporal patterns of population exposure, which can provide references for future adaptation decisions and risk management.

Hosted file

`962871_0_art_file_10964608_r788bp.docx` available at https://authorea.com/users/617561/articles/642939-future-global-population-exposure-to-record-breaking-climate-extremes

Future global population exposure to record-breaking climate extremes

Bohao Li[1,2], Kai Liu[1,3,*], Ming Wang[1], Qianzhi Wang[1,4], Qian He[2], Chenxia Li[5]

[1] School of National Safety and Emergency Management, Beijing Normal University, Beijing 100875, China.

[2] Faculty of Geographical Science, Beijing Normal University, Beijing 100875, China.

[3] Collaborative Innovation Centre on Forecast and Evaluation of Meteorological Disasters (CIC-FEMD), Nanjing University of Information Science & Technology, Nanjing 210044, China

[4] School of Systems Science, Beijing Normal University, Beijing 100875, China.

[5] College of Resources, Environment and Tourism, Capital Normal University, Beijing 100048, China

*Corresponding author: Kai Liu (liukai@bnu.edu.cn)

Key Points:

- Africa and South America will experience successive record-breaking extreme events and even compound drought and heatwaves.
- Population exposure is highly uneven and largely concentrated in underdeveloped areas.
- Record-breaking probability growth is the major driver of population exposure growth in most regions of the world.

Abstract

The increase in record-breaking extreme events caused by climate change poses a threat to human health and well-being; understanding the future impacts of such events on global populations can provide decision-making support for policies aiming to mitigate climate change. Here, we investigated the population exposure to eight climate extreme indices and drivers of exposure trajectories based on NASA Earth Exchange Global Daily Downscaled Projections Coupled Model Intercomparison Project 6 (CMIP6) and population projection data under four shared socioeconomic pathway (SSP) scenarios at a spatial resolution of 0.25°×0.25°. The results show that by the mid-21st century, most regions around the world, especially Africa and South America, will continue to experience record-breaking temperatures and compound drought and heatwaves (CDHWs). Regarding population exposure, under the worst-case scenario of SSP3-7.0 in the late 21st century, the mean value of the multimodel median expected annual exposure (EAE) of all extreme temperature indices and CDHW reaches 8.79 billion persons per year; population exposure hotspots will be concentrated in Central Africa, South Asia, Southeast Asia, and East Asia, mostly in developing countries, where 62.77%-87.42% of the EAE is found. The drivers of exposure trajectories are spatially heterogeneous; the increase in record-breaking probability contributes more than population growth to EAE growth in most regions of the world except Central Asia, the Middle East, and most of Africa. These findings highlight the necessity of using various climate extreme indices to reveal spatiotemporal patterns of population exposure, which can provide references for future adaptation decisions and risk management.

Plain Language Summary

Climate change causes unimaginable increases in extreme weather events that threaten human health and well-being; understanding the future impacts of climate change on global population can inform policies aiming to mitigate climate change. Here, we investigated the spatiotemporal dynamics of future record-breaking extreme temperature and precipitation events, sequential floods and heatwaves (hot extremes after flooding), and compound drought and heatwaves (co-occurring dry and hot extremes) (CDHWs) and analyzed how populations may be potentially affected by these events based on the latest available climate model data and future population projections. The results show that by the mid-21st century, most regions around the world, especially Africa and South America, will continue to experience record-breaking temperatures and CDHWs. Regions where populations will be most affected include Central Africa, South

Asia, Southeast Asia, and East Asia, mostly developing countries. This increase in the affected population is due to the growth of population and the increase of record-breaking extreme events; record-breaking extreme event increase contributes more than population growth in most regions of the world except Central Asia, the Middle East, and most of Africa. These findings confirm the urgent need for adaptive measures and risk management to address future unprecedented climate extremes.

1 Introduction

Increased frequency and intensity of climate extreme events such as droughts, heatwaves, exceptional rainfall or floods caused by climate change have led to heightened human morbidity and mortality and adverse impacts on mental health (Ebi et al., 2021; Grant, 2017). Moreover, climate extreme events have downstream effects that harm human health and well-being by affecting environmental systems, such as increasing the suitability of infectious disease transmission and reducing the yield potentials of major crops (McMichael, 2015; Watts et al., 2021). These implications are usually unequal, with disproportionate impacts on vulnerable populations who contribute the least to the issue, which exacerbates social inequalities (Islam & Winkel, 2017). In extreme event risk management, there is a tendency to adapt most to the highest anomalies in the observed or historical archives, so that record-shattering extreme events often result in significant damage (Fischer et al., 2021); for example, the unprecedented flood that occurred in Zhengzhou, China, in 2021 disrupted the livelihoods of 3.98 million people and killed 16 (Guo et al., 2023), the record-breaking heatwave that occurred in the UK in 2022 killed 3,200 people (Yule et al., 2023), and very extreme climate anomalies that occurred in Europe in 2003 led to persistent droughts and heatwaves resulting in at least 35,000 deaths (Ciais et al., 2005). Exposure is the primary driver of risk and can reflect the situation of people in hazard-prone areas (Kreibich et al., 2022). Accordingly, to ensure adaptive decision-making and risk management, we must investigate the spatiotemporal pattern of future population exposure to record-breaking extreme events to reveal the potential dangers of future extremes.

The above understanding is exceedingly critical and urgent for districts with high urbanization rates and dense populations. Inspired by this concern, several studies have analyzed the spatial and temporal patterns of population exposure to extreme temperature or precipitation under different scenarios based on general circulation model (GCM) simulations (mainly Coupled

Model Intercomparison Project Phase 6 (CMIP6) data) at the global scale (H. Chen & Sun, 2021; Klein & Anderegg, 2021; Park & Jeong, 2022) or identified hotspots of population exposure to climate extremes such as South Asia (Kumar & Mishra, 2020; Zhao et al., 2021), East Asia (W. Zhang & Zhou, 2020), North America (Bryan Jones et al., 2015; Swain et al., 2020), and Africa (Fotso-Nguemo et al., 2023; Iyakaremye et al., 2021). Considering that isolated studies of individual hazards performed through climate risk assessment may underestimate the amplifying effects of multiple extreme event combinations, some studies have been conducted to explore the population exposure to compound events (Das et al., 2022; Wang et al., 2020; G. Zhang et al., 2022). These studies have typically estimated population exposure based on the predicted frequency of future extreme events; however, extreme events have significantly broken long-standing records in recent years, and the occurrence likelihood of record-shattering extremes has increased, making it essential to reveal global population exposure to record-breaking extreme events to assist policymakers in effectively reducing the risk caused by "Black Swan" events (Fischer et al., 2021; Nangombe et al., 2018). Additionally, the spatial resolution of most studies at the global scale is coarser than 1°, and such resolution cannot accurately capture the population exposure variations within different regions; in addition, the use of different climate extreme indices and GCMs makes it difficult to compare population exposure across extreme events. Population exposure projections obtained for various extreme events at high spatial resolution are crucial for facilitating cost-effective investments in adaptation measures and for helping identifying which hazards different regions should prioritize adapting to.

To help decision-makers understand the potential threat to humanity from future global record-breaking extreme events and develop accurate disaster-prevention and disaster-mitigation measures in response to climate change and demographic variations, here, we use the National Aeronautics and Space Administration (NASA) Earth Exchange Global Daily Downscaled Projections CMIP6 (NEX-GDDP-CMIP6) data in combination with future population projection data to analyze the global population exposure to multiple hazards under different future scenarios at a relatively fine spatial resolution (0.25°×0.25°). The objectives of this study are specified as follows: (1) to quantify hazards using climate extreme indices and demonstrate the spatiotemporal dynamics of global future record-breaking probabilities for different indices under each scenario; (2) to compare global future population exposures to different climate extreme indices in different decades of the 21st century under each scenario globally and reveal hotspots of population exposure in the late 21st century; and (3) to investigate population exposure trajectories and quantify how record-breaking probability and future population drive exposure trajectories in different regions.

2 Materials and Methods

2.1 NEX-GDDP-CMIP6

The NEX-GDDP-CMIP6 dataset provides global downscaled climate scenarios derived from CMIP6 GCM simulations at a spatial resolution of 0.25°×0.25° (approximately 25 km) generated based on the bias-correction spatial disaggregation method (Wood et al., 2004). This dataset consists of 35 GCMs at the daily scale, including simulations of the historical period (1950-2014) and four scenario composites that represent combined Shared Socioeconomic Pathway (SSP) and Representative Concentration Pathway (RCP) scenarios (SSP1-2.6, SSP2-4.5, SSP3-7.0, and SSP 5-8.5) for the future (2015-2100) (O'Neill et al., 2016). Most GCMs produce data that include nine meteorological variables (Thrasher et al., 2022). In this study, we used 22 GCMs, all of which contained four SSP scenarios and key meteorological variables, including the near-surface relative humidity (hurs), precipitation (pr), daily near-surface air temperature (tas), daily maximum near-surface air temperature (tasmax), and daily minimum near-surface air temperature (tasmin) (Table S1); the SSP3-7.0 results were highlighted for analysis in this study, and the multimodel median was used for the spatiotemporal characterization. Table 1 provides brief descriptions of the scenarios used in this study.

Table 1. Description of climate scenarios considered in this study.

Scenario name	Forcing category	Global warming by 2100 compared to the preindustrial level	Description
SSP1-2.6	Low	1.8 °C	This pathway uses sustainable development policies and represents the low end of the future forcing pathways
SSP2-4.5	Medium	2.7 °C	SSP2-4.5 envisages an intermediate path in which the historical development pattern is continued
SSP3-7.0	High	3.6 °C	This pathway represents increased social inequality, rapid population growth, low investments in education and health, and relatively high forcing

SSP5-8.5	High	4.4 °C	This pathway assumes a fossil-based, energy-intensive economic development pattern, representing a very high emission scenario

2.2 Gridded population data

Jones & O'Neill (2016) produced grid cell-level population projections for five SSPs, SSP1, SSP2, SSP3, SSP4, and SSP5, from 2010 to 2100 at a 10-year interval using the parameterized gravity-based downscaling model; the data had a spatial resolution of 0.125°×0.125°. In this study, we used population projection data for the 2020-2100 under the four SSPs in Table 1 and resampled the data to 0.25°×0.25° using a weighted summation method to match the NEX-GDDP-CMIP6 data. Figure S1 shows the population trends from 2020 to 2090.

2.3 Climate reference regions

To better illuminate the spatiotemporal patterns of regional record-breaking probability and population exposure for better understanding by citizens and scientists, we analyzed the key results at a subcontinental scale based on climate reference regions (Figure S2) that take into account precipitation and temperature distribution characteristics, as used by the Intergovernmental Panel on Climate Change (IPCC) Sixth Assessment Report (AR6) (Iturbide et al., 2020).

2.4 Climate extreme indices

We selected eight climate extreme indices that are relevant to human health and livelihoods (Table 2). Three extreme precipitation indices, including the total precipitation (PRCPTOT), maximum 1-day precipitation (RX1D), and number of days with heavy precipitation (R50), were used to reflect the frequency and intensity of global precipitation. Three extreme temperature indices, including warm days (Tx90p), warm nights (Tn90p), and heatwaves (HW), were considered to analyze the effect of diurnal and consecutive heat extremes on public health. We considered two types of compound events: sequential flood-heatwave (SFH) and compound drought and heatwave (CDHW). The selection of these two compound indices was based on the following concerns: extreme flooding may be closely associated with extreme heat, and the electricity supply outages caused by floods make post-flood humid-heat events more likely to trigger heat stress (Gu et al., 2022); and drought triggers wildfires that cause air pollution and damage crops, thereby increasing the number of heatwave-related fatalities (Zscheischler et al., 2018). Here, the weighted average of precipitation (WAP) (Lu, 2009) is intended as a proxy for pluvial floods and is calculated as shown in Eq. 1:

$$WAP = (1 - a) \sum_{n=0}^{N} a^n P_n \#(1)$$

where the parameter a = 0.9; we calculate the index in years, with N representing the number of days counting backward to the beginning of a year, n is the nth day of the year, and Pn is the daily precipitation on the nth day of the year. After a flood, the relatively high humidity may exacerbate human discomfort resulting from the effects of extreme heat, so we use the heat index (HI) (Anderson et al., 2013) instead of the daily maximum temperature to account for the SFH; the HI calculation formula is adopted from the National Weather Service (NWS) (NWS, 2011), and HI >40.6°C is classified as extreme heat taking into account humidity in this study (Lin, 2019). According to Chen et al. (2021), an SFH is defined as a consecutive occurrence of floods and heatwaves within a week. Drought events are identified using the standardized precipitation evapotranspiration index (SPEI) (Vicente-Serrano et al., 2010) on a 3-month time scale; CDHWs are considered as the frequency of heatwaves occurring during drought months (SPEI <-1) (Yin et al., 2023; Q. Zhang et al., 2022). Based on the python climate-indices library, we calculate the monthly potential evapotranspiration (PET) using the Thornthwaite method (Thornthwaite, 1948) and the monthly near-surface air temperature data; then, we input the monthly PET and precipitation data to calculate SPEI. All indices are counted as annual time series. Table 2 shows the definitions of the climate extreme indices used in this study.

Table 2. The climate extreme indices chosen for this study

Category	Label	Index name	Definition	Unit
Extreme precipitation	PRCPTOT	Total precipitation	Annual total precipitation	mm
	RX1D	Maximum 1-day precipitation	Annual maximum 1-day precipitation	mm
	R50	Number of days with heavy precipitation	Number of days with daily precipitation >50 mm in a year	days
Extreme temperature	Tx90p	Warm days	Number of days with maximum temperature >90th percentile of the	days

			historical period in a year	
	Tn90p	Warm nights	Number of days with minimum temperature >90th percentile of the historical period in a year	days
	HW	Heatwave	Number of times in a year when the maximum temperature >90th percentile of the historical period for more than 3 consecutive days	times
Compound events	SFH	Sequential flood-heatwave	Number of successive occurrences of floods (WAP >95th percentile of the historical period) and heatwaves (HI >40.6 °C for more than 3 consecutive days) within a week in a year	times
	CDHW	Compound drought and heatwave	Number of heatwaves (maximum temperature >90th percentile of the historical period) coinciding with monthly drought events (SPEI <-1) in a year	times

2.5 Record-breaking probability

For each annual time series of extreme climate indices, a record-breaking year is defined as a year in which the maximum value recorded during the historical period is exceeded; the annual record-breaking probability is calculated as the proportion of the record-breaking years in a given future period. We derived record-breaking probabilities on a grid scale for the late-21st century (2071-2100) and at decadal intervals from the 2020s to 2090s (for example, 2015-2024 for the 2020s and 2085-2094 for the 2090s).

2.6 Population exposure

2.6.1 Exposure definitions

In this study, the annual population exposure refers to the population in a record-breaking year; combining record-breaking probabilities and population data, we use the expected annual exposure (EAE) to reveal the spatiotemporal distribution and dynamics of population exposure in persons per year, as obtained from Eq. 2:

$$EAE_T = Prob_T \times \frac{\sum_{n=0}^{N} Pop_n}{N} \#(2)$$

where T is the future period, $Prob$ is the record-breaking probability, Pop_n is the nth available population data in T , and N represents the number of available population data in T. Matching the record-breaking probabilities, gridded population exposures are generated for the late-21st century and the 2020s to 2090s at decadal intervals.

2.6.2 Exposure contributions

To investigate the importance of the population and record-breaking probability in the exposure trajectory, we quantified the shares of the population and record-breaking probability from the 2020s to 2090s in EAE using Eq. 3 and Eq. 4 as follows:

$$EAE_{T,prob} = Prob_T \times Pop_{2020} \#(3)$$

$$EAE_{T,pop} = Prob_T \times \left(\frac{\sum_{n=0}^{N} Pop_n}{N} - Pop_{2020}\right) \#(4)$$

where $EAE_{T,prob}$ and $EAE_{T,pop}$ are the share of the record-breaking probability and the population to EAE_T, respectively, and Pop_{2020} refers to the population in 2020.

2.6.3 Exposure trends

Simple ordinary least squares (OLS) linear regression models were considered in this study to estimate the population exposure trends; to obtain the rate of change in exposure, we only retained areas with statistically significant increases ($p < 0.05$). We estimated the population exposure trends in persons per decade from the 2020s to 2090s and calculate the contributions of population increase and record-breaking probability increase to the variation in population exposure.

3 Results

3.1 Spatial and temporal patterns of global record-breaking probabilities

By the late-21st century, the spatial distribution patterns of record-breaking probabilities of extreme precipitation indices, HWs, and SFHs, are very similar under all four scenarios, while Tx90p, Tn90p, and CDHWs vary considerably across the four scenarios (Figure 1 and Figure S3-S5). Under the SSP3-7.0 scenario, the PRCPTOT record-breaking hotspots are concentrated on the Tibetan Plateau (TIB) and in the high-latitude regions of the Northern Hemisphere, including Alaska, Canada, the Arctic, and Northern Asia (NAS), with average record-breaking probabilities of 13.4% and 16%, respectively (Figure 1a). The areas with the highest record-breaking probability of RX1D are mainly located in Central Africa (CAF) and Southeast Asia (SEA), both of which have 35% of the grid cells exceeding 10% probability (Figure 1b). In CAF and South Asia (SAS), where the R50 record-breaking probability is relatively high, only 9.6% and 10.6% of the grid cells' probability exceed 10%, respectively (Figure 1c). The record-breaking probabilities for Tx90p and Tn90p are extremely high, with global averages of 91.6% and 98.8%, meaning that almost the entire globe will be continuously affected by record-breaking extreme temperatures (Figure 1d and 1f). Most regions south of 30°N will experience a high record-breaking probability of HWs, especially in northern South America (NSA) and CAF, with averages of 39.1% and 34.6%, respectively (Figure 1e). The spatial variability in SFHs is high, with record-breaking probabilities exceeding 50% mainly in CAF, the TIB, SAS, and SEA, corresponding to 8.5%, 4.8%, 4.8%, and 4% of the grid cells, respectively; however, 68-81% of the grid cells in these regions have probabilities less than 10% (Figure 1g). CDHWs will have an overall high record-breaking probability south of 40°N, especially on the TIB and in Central America, Mexico, and the Caribbean (CAMC), Central Asia (CAS), SAS, and the Sahara (SAH), with average probabilities ranging from 52.5%-85.1%.

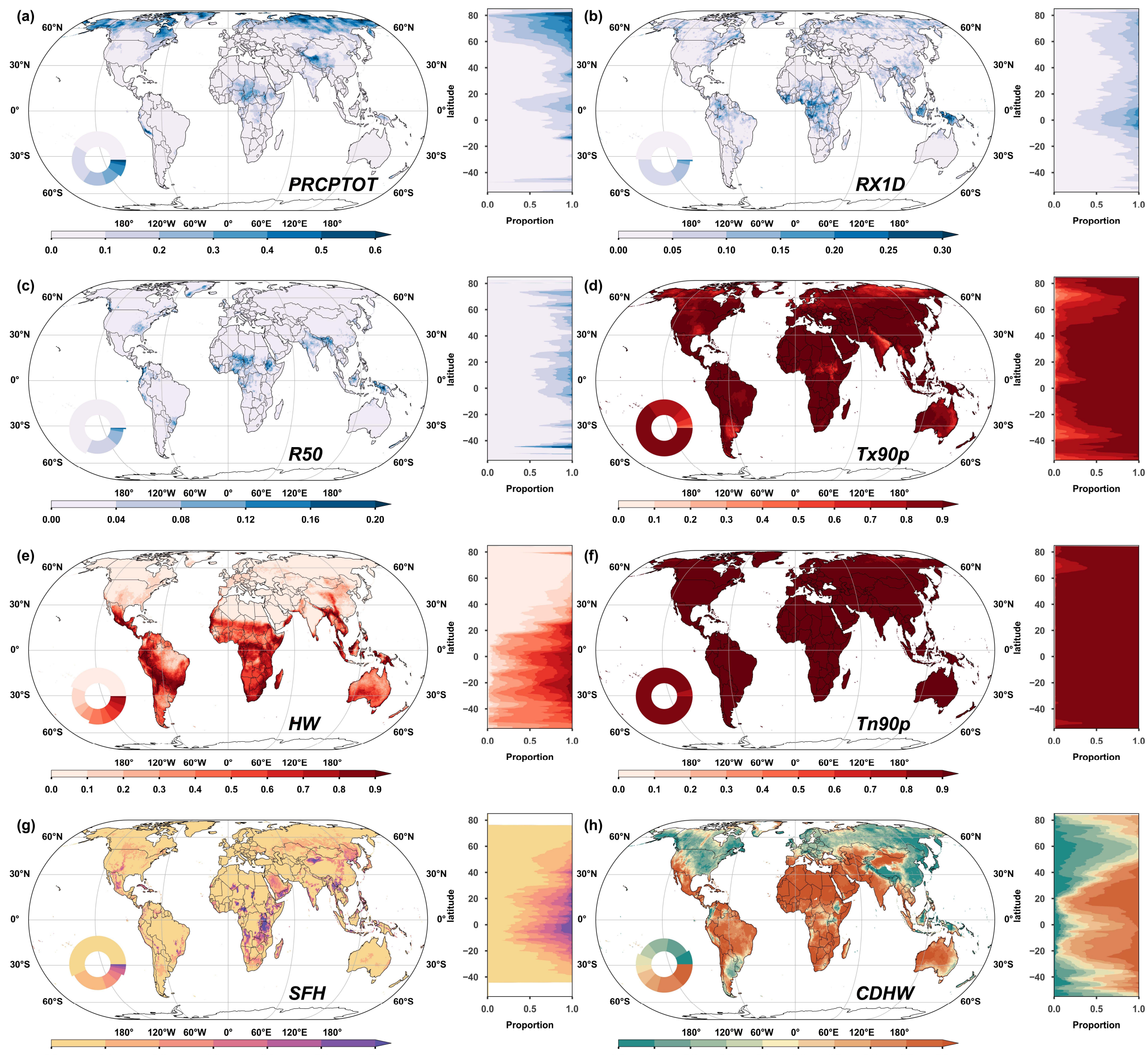

Figure 1 Annual record-breaking probability projections of multimodel medians for different climate extreme indices in the SSP3-7.0 scenario for the late-21st century: (a) PRCPTOT, (b) RX1D, (c) R50, (d) Tx90p, (e) HW, (f) Tn90p, (g) SFH, and (h) CDHW. The rings show the percentages of pixels corresponding to different record-breaking probability levels; the stacked charts demonstrate the proportions of the record-breaking probability levels at different latitudes.

In dynamic terms, the record-breaking probabilities of all climate extreme indices show local or nearly global increases from the 2020s to the 2090s under different scenarios, except the extreme precipitation indices and SFHs, which do not change significantly under the SSP1-2.6 scenario (Figure 2 and S6-S8). Figure S8 illustrates the record-breaking probability trends corresponding to the indices under the SSP3-7.0 scenario. Record-breaking probabilities of extreme precipitation will increase relatively slowly; the PRCPTOT growth rates exceed 5% per decade in parts of the high-latitude Northern Hemisphere and on the TIB; RX1D and R50 both grow at less than 5% per decade globally (Figure S8 a-c). The global average record-breaking probability growth rates of Tx90p, Tn90p, and CDHW amount to 13.3%, 11.1%, and 8.3% per decade, respectively; these results indicate that most regions of the world will be continuously exposed to record-breaking heat events and even CDHWs by the middle of the 21st century (Figure S8d, f, and h). The HW record-breaking growth hotspots are Australia and New Zealand (ANZ), CAMC, CAF and Southern Africa (SAF), with average growth rates of 7.1%, 8.3%, 8.9%, and 10.1% per decade, respectively (Figure S8e). Although the global average SFH record-breaking probability rate is not high, some regions will experience rapid growth (over 10% per decade), primarily CAF and Asia (Figure S8g).

3.2 Global population exposure to climate extremes

Figure 2 depicts the total global multimodel EAE projections from the 2020s to 2090s. The changes in EAE for extreme precipitation are very similar under different scenarios, with the EAE increasing gradually with time for PRCPTOT and RX1D and remaining almost constant for R50; under the two high-emission scenarios, the multimodel median EAE for PRCPTOT and RX1D will reach 0.69 billion and 0.50 billion persons per year under the SSP3-7.0 scenario, respectively, and 0.56 billion and 0.43 billion persons per year under the SSP5-8.5 scenario, respectively, by the 2090s (Figure 2a-c). The EAE trends for extreme temperature and compound events vary considerably across the four scenarios; under the SSP2-4.5 and SSP3-7.0 scenarios, the global EAE of all indices except Tn90p continues to increase from the 2020s to the 2090s, while under the SSP1-2.6 and SSP5-8.5 scenarios, the global EAE growth rate slows down after the 2050s and even declines by the end of the 21st century (Figure 2d-h). Under the SSP3-7.0 scenario, the EAEs in the 2090s are very high for Tx90p, HW, Tn90p, and CDHW, with the multimodel medians reaching 11.31 billion, 3.84 billion, 12.11 billion, and 7.88 billion persons per year, respectively. The mean value of the multimodel medians of these four temperature extreme indices reached 1.64-1.95 times the mean values of the multimodel medians of all indices under different scenarios over time. The global population exposure to climate extremes under the SSP3-7.0 scenario is more pronounced than that under other scenarios; this is inextricably linked to the high population growth rates and emissions. Although the population exposure to extreme precipitation is clearly lower than that to extreme temperature, the impacts of extreme precipitation cannot be ignored, as extreme precipitation acts as a trigger for compound events that pose more serious hazards to humans, such as SFHs and CDHWs.

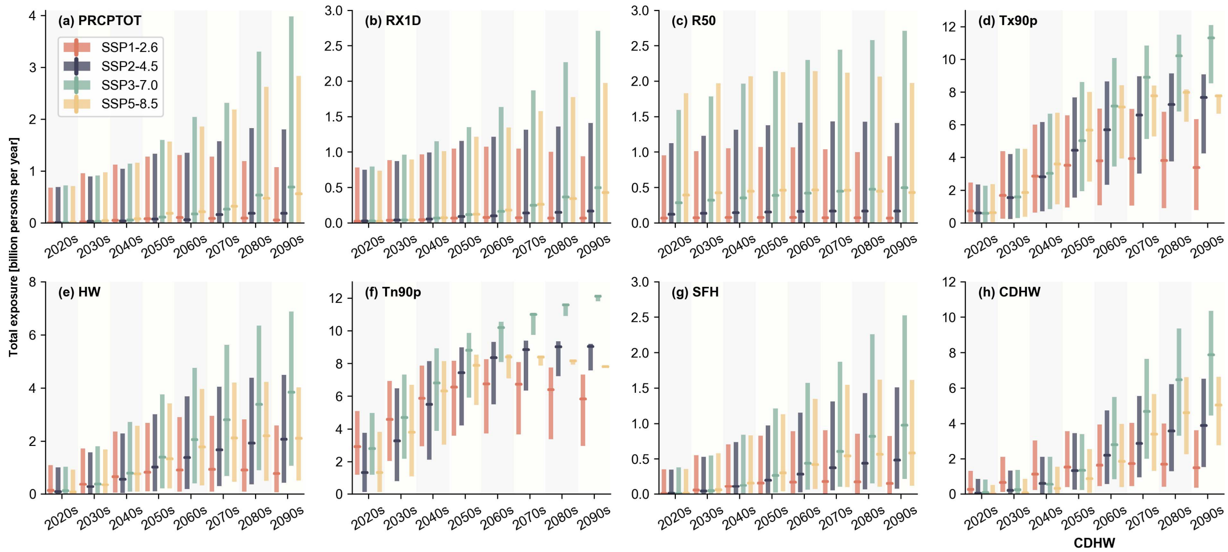

Figure 2 Total global EAE projections for different climate extreme indices under four scenarios from the 2020s to 2090s: (a) PRCPTOT, (b) RX1D, (c) R50, (d) Tx90p, (e) HW, (f) Tn90p, (g) SFH, and (h) CDHW. The range of bars refers to the multimodel 10th-90th percentiles of the EAE; the solid line in the middle is the multimodel median. The unit of total exposure is billon persons per year.

Figures 3 and 4 show the results of the global EAE projections for the late-21st century under the SSP3-7.0 scenario. Regions with high population exposure to all indices are concentrated in low and middle latitudes, mainly CAF, SAS, SEA, and East Asia (EAS); these areas contribute 62.77%-87.42% to the EAE with 65.32% of the global population. Both CAF and SAS have very high EAEs for PRCPTOT, with the higher EAEs in CAF identified mainly in the western, eastern, and southeastern regions, while almost the whole region of India in SAS has high EAEs; 13.47% and 37.8% of the grid cells in CAF and SAS, respectively, indicate exposures greater than 30,000 people per year (Figure 3a). The EAE hotspot areas for RX1D are similar to those for PRCPTOT, but RX1D has fewer high-EAE areas in CAF, SAS, and EAS (Figure 3b). The regions with high EAEs for R50 are clustered in CAF and SAS, with 6.97% and 21.75% of the grid cells in these regions having EAEs greater than 30,000 persons per year, respectively, while in other regions, such as the middle and high latitudes of the Northern Hemisphere, ANZ, and South America, the EAEs are very low (Figure 3c). Since Tx90p and Tn90p have very high record-breaking probabilities in the late-21st century, the global EAE to the two indices is almost identical to the global population distribution, with the EAEs of CAF, SAS, and EAS all exceeding 800 million people per year (Figures 3d and f). The spatial distribution pattern of the EAE of CDHW is very similar to that of Tx90p; the only difference is that CDHWs have very low EAEs in the EAS (Figure 3h). The EAE hotspots for HW are primarily located in CAF, the border regions of India in SAS, and SEA, where 20.53%, 16.94%, and 10.03% of the grid cells have EAEs exceeding 100,000 people per year, respectively; although the EAEs of Tx90p are high in east-central China, the EAEs of HW are relatively low (Figure 3e). SFHs have high EAEs in CAF, SAS, SEA, and EAS, with 6.44%, 4.81%, 3.55%, and 0.70% of the grid cells having EAEs surpassing 100,000 people per year, respectively; notably, the population exposure of SFH in EAS is almost exclusively located along the Hu Huanyong Line in China (Figure 3g).

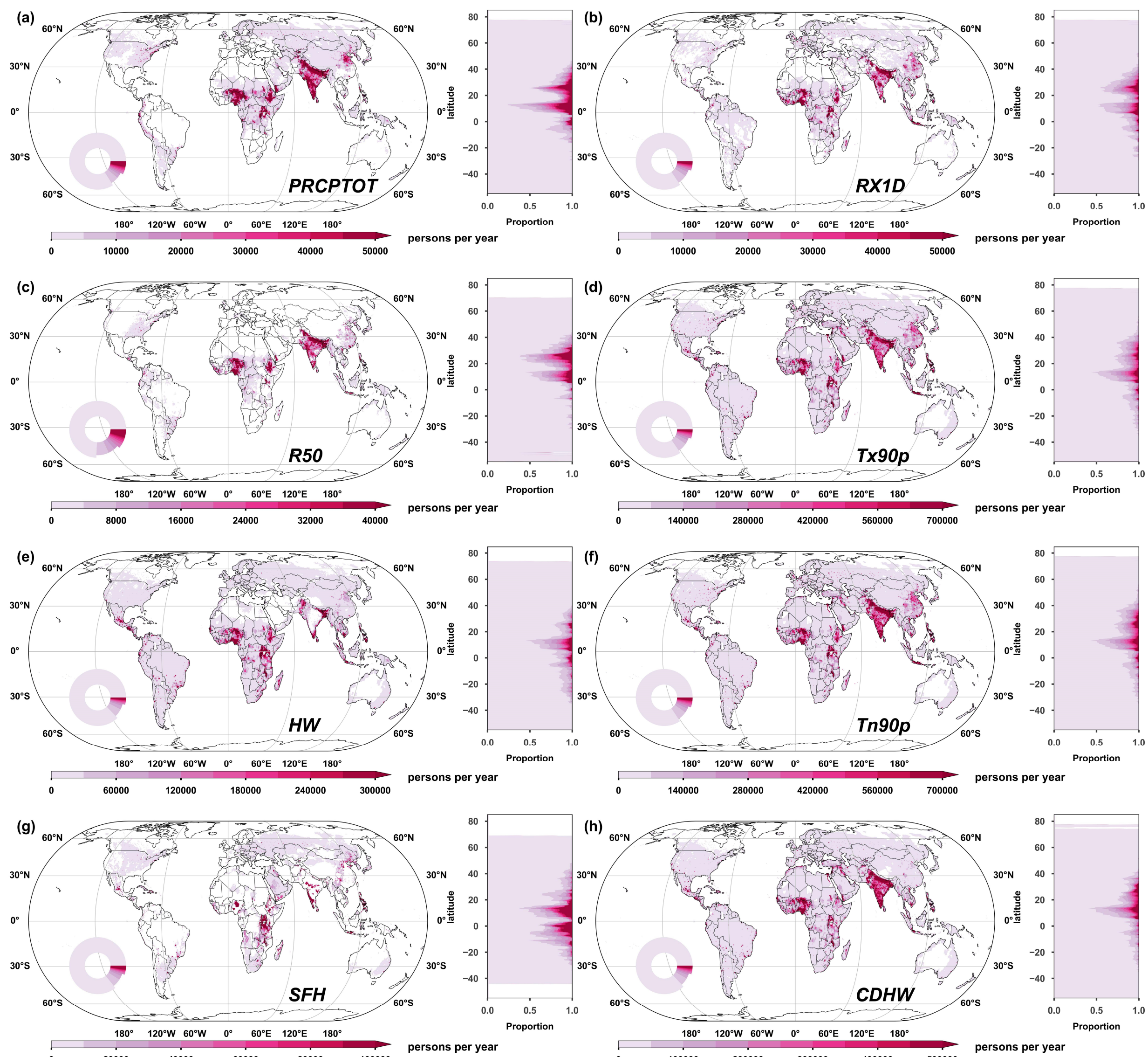

Figure 3 EAE projections of multimodel medians for different climate extreme indices in the SSP3-7.0 scenario for the late-21st century: (a) PRCPTOT, (b) RX1D, (c) R50, (d) Tx90p, (e) HW, (f) Tn90p, (g) SFH, and (h) CDHW. The rings show the percentages of pixels corresponding to different population exposure levels; the stacked charts demonstrate the population exposure proportion at each level at different latitudes.

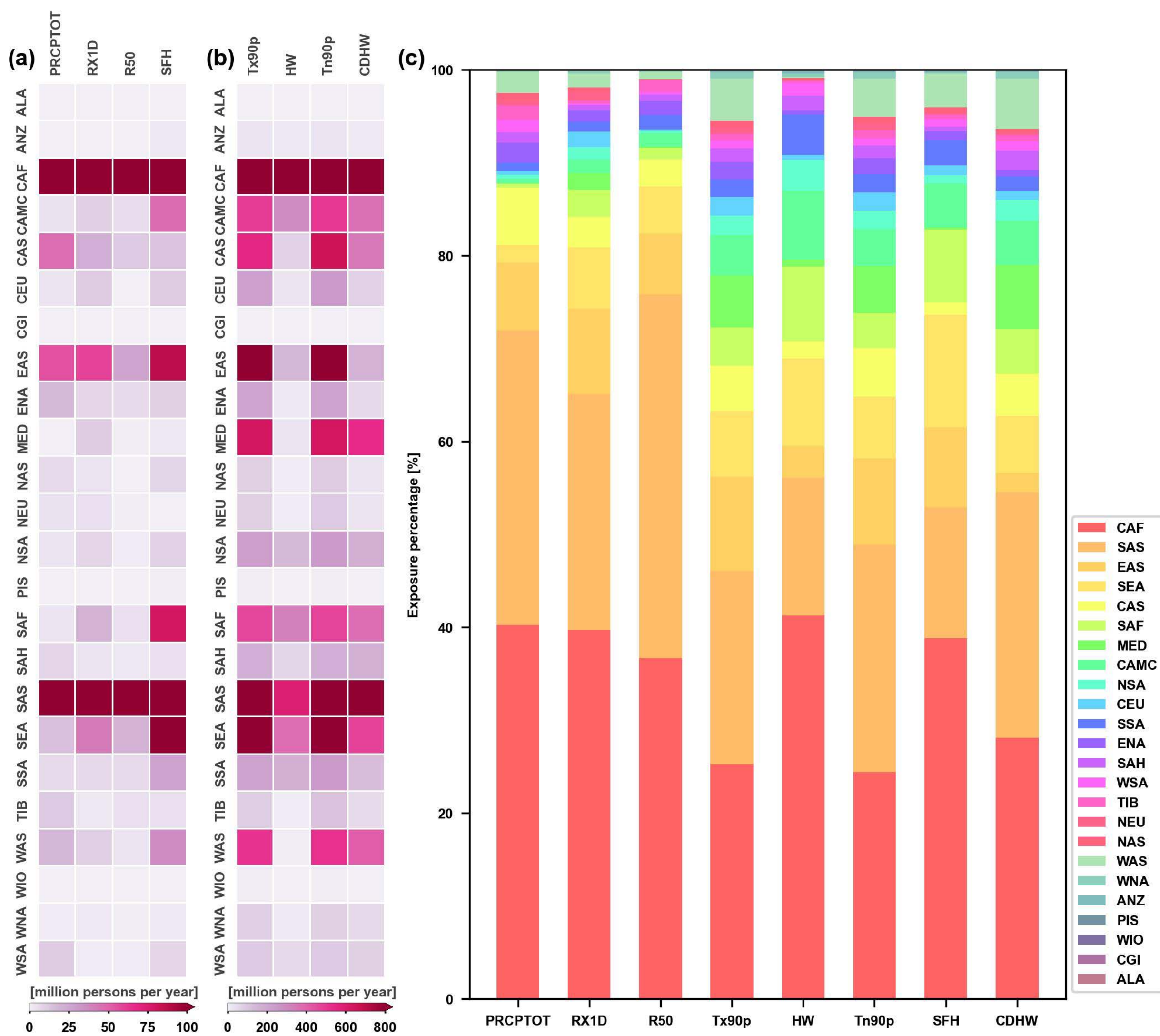

Figure 4 Subcontinental EAE projections of the multimodel medians for different climate extreme indices in the SSP3-7.0 scenario for the late-21st century: (a) PRCPTOT, RX1D, R50, SFH, (b) Tx90p, HW, Tn90p, CDHW, and (c) regional percentages of the total global EAE.

We calculated the EAEs under other scenarios in the late-21st century and derived essentially the same spatial population exposure pattern in the different scenarios (Figure S10-15). The global EAEs for all climate extreme indices under SSP3-7.0 are 2.35-8.32, 1.44-3.05, and 1.34-1.97 times higher than those under SSP1-2.6, SSP2-4.5, and SSP5-8.5, respectively (Table S2). SAS has the largest EAE variation among all the subcontinental regions across all scenarios; under the

SSP1-2.6 scenario, SAS has an evidently lower global share of EAE for most indices compared to other scenarios.

3.3 Population exposure trends and exposure trajectory drivers

Figure S18 demonstrates the spatial distribution of the global EAE growth rates under the SSP3-7.0 scenario, with hotspot areas similar to those of the EAE in the late-21st century. The EAEs of certain indices exhibit relatively low growth rates in some regions, but high EAEs are still expected by the late-21st century, which is the case for RX1D in northeast India, R50 in China and India, and Tn90p in southern China. These regions have typically experienced high EAEs in the 2020s, thus increasing the need for measures to combat weather extremes and protect citizens. We analyzed the global EAE trends under the other scenarios and concluded that the global EAE growth rates for different indices under the SSP3-7.0 scenario are 3.52-59.98, 1.21-6.76, and 0.96-1.70 times higher than those under the SSP1-2.6, SSP2-4.5, and SSP5-8.5 scenarios, respectively (Table S3) (Figure S16-S19).

Figure 5 demonstrates a strong spatial divergence pattern in the shares of record-breaking probability increase rates and population increase rates to EAE growth rates for all indices under the SSP3-7.0 scenario. In CAS, the Middle East in West Asia (WAS), and the majority of Africa, population growth contributes more than record-breaking probability growth; except these regions, most of the global region is dominated by record-breaking probability growth driving EAE growth. Under the SSP3-7.0 scenario, the contribution of record-breaking probability growth rates to EAE growth rates under different indices ranges from 48.75% to 62.30%, and this scenario predicts the lowest contribution of record-breaking probability growth rate to the EAE growth rate. The shares of record-breaking probability growth rates under the SSP1-2.6, SSP2-4.5, and SSP5-8.5 scenarios are 1.59-2.07, 1.27-1.51, and 1.50-1.83 times higher than that under the SSP3-7.0 scenario, respectively (Table S4) (Figures S20-22).

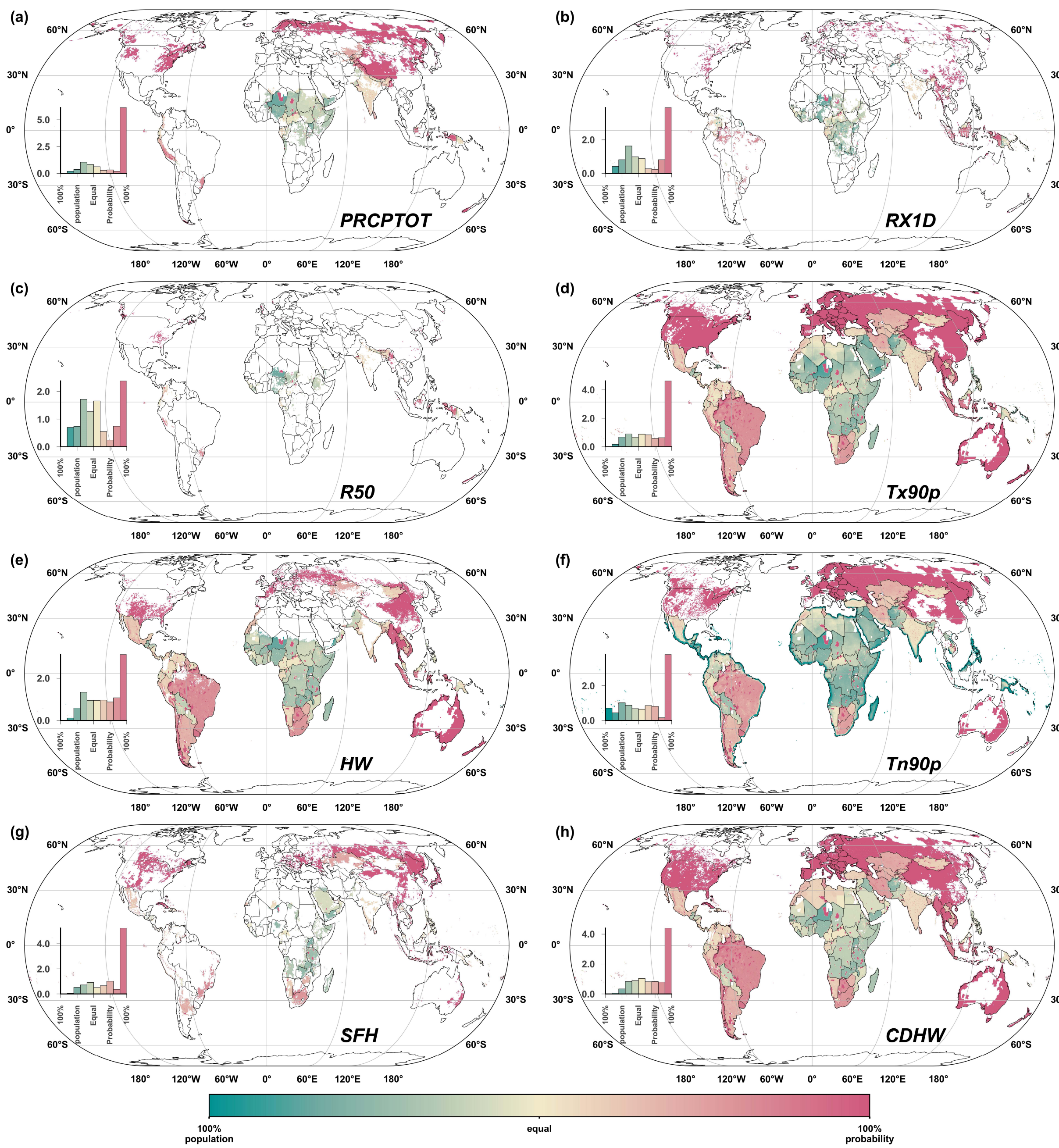

Figure 5 Contributions of record-breaking probability growth and population growth to the multimodel median EAE growth rates for different climate extreme indices projected under the SSP3-7.0 scenario: (a) PRCPTOT, (b) RX1D, (c) R50, (d) Tx90p, (e) HW, (f) Tn90p, (g) SFH, and (h) CDHW. The histograms depict the probability densities at different contribution levels.

Next, we detailed how the EAEs are expected to change from the 2020s to the 2090s in different regions of the globe at subcontinental scales and analyze how signals from demographics and record-breaking probabilities drive the exposure trajectories in each region (Figure 6 and Figures S23-25). Under the SSP3-7.0 scenario, the EAEs for different indices are predicted to increase considerably in most regions of the world, with the EAEs in CAF and SAS for PRCPTOT, RX1D, R50, and SFH experiencing growth rates exceeding 10 million persons per decade, and for Tx90p, HW, Tn90p, and CDHW having EAE growth rates over 100 million persons per decade (Figure 6a and b). CAF and SAS, two regions with similar exposure trajectories, differ sharply in the importance of the demographic condition and record-breaking probabilities to the EAE growth rates; the share of record-breaking probability growth in CAF ranges from 67.52% to 76.93% for different climate extreme indices, while the share of record-breaking probability growth in SAS ranges from only 40.04% to 53.82% (Figure 6c). In addition, regions with negative or slight variations in the population growth rate (Figure S1 c), as represented by the EAS, have exposure trajectories driven entirely by record-breaking probabilities. Some indices have very high record-breaking probabilities as early as the 2020s and very low record-breaking probability increase rates, and thereby exposure trajectories are dominated by population changes; for example, Tn90p is prone to break records in coastal regions such as the West Indian Ocean (WIO) and Pacific Islands (PIS), where the share of population growth is 100%. Uncovering the spatially distinct patterns of exposure trajectory drivers is essential because such differences can effectively assist decision-makers in understanding the costs and benefits of local adaptations (Estrada et al., 2017; Tuholske et al., 2021).

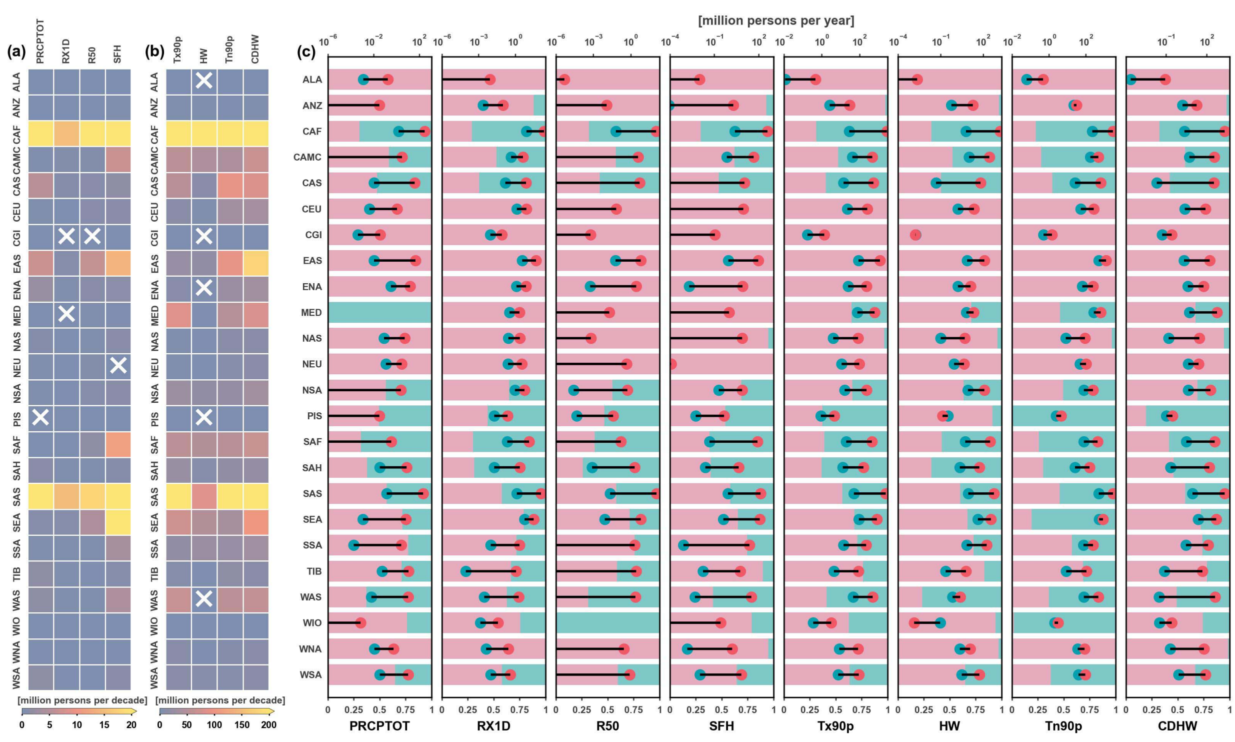

Figure 6 Subcontinental multimodel median EAE variations under the SSP3-7.0 scenario for different climate extreme indices from the 2020s to 2090s: (a) EAE growth rates for PRCPTOT, RX1D, R50, and SFH, (b) EAE growth rates for Tx90p, HW, Tn90p, and CDHW, and (c) shares of the population growth and record-breaking probability growth contributing to the EAE increase in the 2020s and 2090s. The "×" symbols in panels (a) and (b) denote nonsignificant EAE growth (p value <0.05).

To capture the drivers of exposure trajectories within typical regions at the subcontinental scale, we selected the regions with the top three multimodel median EAE growth rates for each climate extreme index under the SSP3-7.0 scenario to demonstrate the distribution of drivers of EAE growth rates (Figure S26). The distributions of the exposure trajectories of the different climate extreme indices are very similar within the same region, and for each index, the spatial variability of exposure trajectories is high within the regions. CAF and SAS both have very high population growth rates; the shares of these two drivers are similar in most of the SAS region, and the share of the record-breaking probability increase is greater than that of the population growth in a few SAS regions, while population growth rates dominate the exposure trajectories in most of CAF. The increase in EAE within EAS will be caused almost entirely by increased record-breaking probability due to negative population growth. In approximately half of the SEA region, the two drivers have similar shares, while in the other half of the region, the exposure trajectory is dominated by record-breaking probability. CDHWs have relatively high EAE growth rates in South Europe and the Mediterranean (MED), where the exposure trajectory will be almost entirely driven by record-breaking probability increases in about half of the MED (mainly northern Europe), and the share of the two drivers will be similar in the other half (mainly Northern Africa).

4 Discussion and Conclusion

In this study, we used NEX-GDDP-CMIP6 data to derive the record-breaking probabilities of eight climate extreme indices from 22 GCMs under four scenarios; we then analyzed the spatiotemporal dynamics of population exposure in conjunction with population projection data and analyzed the drivers of the derived exposure trajectories. We found that the accelerated development of relatively high emissions will significantly increase the global record-breaking probabilities of extreme events. The record-breaking probabilities of extreme precipitation events and SFHs are expected to increase at much lower rates than extreme temperature events and CDHWs. Except for the SSP1-2.6 scenario, where almost no increase in the global record-breaking probability of extreme precipitation events or SFHs is predicted, all climate extreme indices show some increase in record-breaking probabilities in different regions of the world under the different scenarios analyzed herein. The population exposure in the late 21st century is expected to be very high under the SSP3-7.0 scenario, with the multimodel medians of different indices being 2.35-8.32, 1.44-3.05, and 1.34-1.97 times higher than those obtained under the SSP1-2.6, SSP2-4.5, and SSP5-8.5 scenarios, respectively. The population exposure to extreme precipitation events and SFHs is much smaller than that to extreme temperature events and CDHWs. In the late 21st century, most of the EAEs under all scenarios will be concentrated in CAF, SAS, SEA, and EAS, except under the SSP5-8.5 scenario, where East North America (ENA) will be another population exposure hotspot. Although the SSP5-8.5 scenario conferred the highest record-breaking probabilities of extreme events, the population exposure under this scenario is expected to be much lower than that under SSP3-7.0, reflecting the fact that management policies regarding population development will significantly impact the future population exposure. Understanding the drivers of future exposure trajectories is particularly important for risk management. Here, we provide a detailed explanation of the spatial heterogeneity corresponding to the ways in which population and record-breaking probability are expected to drive global population exposure trajectories. In all four scenarios analyzed in this study, the share of record-breaking probability increases to the global population exposure growth is higher than the share of population growth, with only the SSP3-7.0 scenario predicting a relatively high share of population growth. In CAS, the Middle East in WAS, and the majority of Africa, the exposure trajectories will be predominantly population-driven, while in other regions, the exposure trajectories will be mainly record-breaking probability-driven.

Although our study focuses on population exposure to record-breaking extreme events and our results cannot be compared directly to previous work performed at the global or regional scales, the population exposure hotspots identified in this study mostly correspond to areas with high population exposure to extreme events, such as CAF, SAS, and EAS in previous studies. There are certain limitations and potential improvements to this study. First, we ignored demographic characteristics, such as age, gender, education, and income, which can indicate the vulnerability of the population and influence the mortality rate of population affected by climate extremes; this is a common problem faced in relevant studies, and few comparable historical datasets are available to provide vulnerability information in large-scale studies (Coffel et al., 2017;

Iyakaremye et al., 2021; Weber et al., 2020). In addition, we used the extreme state of the WAP to represent flooding, and this assumption lacks consideration of non-precipitation factors such as land cover and flood management infrastructure. A combination of extreme indices and hydrodynamic models may allow for better flood predictions (Y. Chen et al., 2021). We concentrated only on extreme heat and extreme humid-heat events while ignoring other meteorological features, such as wind speed and solar radiation that may impact humans. The use of multiple location-based heat indices can forge good synergies for research domains such as the global scale considered herein (Tuholske et al., 2021; Vanos et al., 2020). As socioeconomic development increases the awareness of and preparedness for extreme events, there is a need to dynamically consider the historical record of extreme events to accurately capture future record-breaking probabilities. The definitions of the climate extreme indices and record-breaking probabilities used in this study somewhat diminished the impacts of extreme event intensities. Designing some metrics that quantify both the intensity and frequency of extreme events could effectively solve this issue (Q. Zhang et al., 2022). Moreover, there is uncertainty in the projection data used in this study. Gridded population projections ignore the potential impacts of climate change, such as extreme drought-induced migration, which will be a priority issue in the future (B. Jones & O'Neill, 2016). We used many GCMs to perform a comparative analysis of multiple extreme events, but the predictions of future climate patterns varied considerably among GCMs, especially the predictions of precipitation patterns. Applying optimal bias-correction methods could reduce this uncertainty (Coffel et al., 2017; Levy et al., 2013).

The global population exposure to extreme events is highly unequal, with developing countries in particular having much greater population exposures than developed countries. While we must strive to keep the development pathway in accordance with the SSP1-2.6 scenario to prevent serious impacts from climate change, addressing socioeconomic and infrastructure issues through adaptation measures and financial assistance will be effective in reducing the damages caused by climate change. For developing countries, it will certainly be a challenge to manage risks with the limited funds available. The findings of this study could help drive future policy-making related to climate change mitigation and controlling population growth to ensure a sustainable future worldwide.

Acknowledgements

This work was supported by the National Natural Science Foundation of China (grant number 41771538). The financial support is highly appreciated.

Open Research

The data used in this study is available at https://doi.org/10.6084/m9.figshare.22767122.v1.

The NEX-GDDP CMIP6 dataset can be accessed at https://www.nccs.nasa.gov/services/data-collections/land-based-products/nex-gddp-cmip6.

References

Anderson, G. B., Bell, M. L., & Peng, R. D. (2013). Methods to Calculate the Heat Index as an Exposure Metric in Environmental Health Research. Environmental Health Perspectives, 121(10), 1111–1119. https://doi.org/10.1289/ehp.1206273

Chen, H., & Sun, J. (2021). Significant Increase of the Global Population Exposure to Increased Precipitation Extremes in the Future. Earth's Future, 9(9), e2020EF001941. https://doi.org/10.1029/2020EF001941

Chen, Y., Liao, Z., Shi, Y., Tian, Y., & Zhai, P. (2021). Detectable Increases in Sequential Flood-Heatwave Events Across China During 1961–2018. Geophysical Research Letters, 48(6), e2021GL092549. https://doi.org/10.1029/2021GL092549

Ciais, P., Reichstein, M., Viovy, N., Granier, A., Ogée, J., Allard, V., et al. (2005). Europe-wide reduction in primary productivity caused by the heat and drought in 2003. Nature, 437(7058), 529–533. https://doi.org/10.1038/nature03972

Coffel, E. D., Horton, R. M., & Sherbinin, A. de. (2017). Temperature and humidity based projections of a rapid rise in global heat stress exposure during the 21st century. Environmental Research Letters, 13(1), 014001. https://doi.org/10.1088/1748-9326/aaa00e

Das, J., Manikanta, V., & Umamahesh, N. V. (2022). Population exposure to compound extreme events in India under different emission and population scenarios. Science of The Total Environment, 806, 150424. https://doi.org/10.1016/j.scitotenv.2021.150424

Ebi, K. L., Vanos, J., Baldwin, J. W., Bell, J. E., Hondula, D. M., Errett, N. A., et al. (2021). Extreme Weather and Climate Change: Population Health and Health System Implications. Annual Review of Public Health, 42(1), 293–315. https://doi.org/10.1146/annurev-publhealth-012420-105026

Estrada, F., Botzen, W. J. W., & Tol, R. S. J. (2017). A global economic assessment of city policies to reduce climate change impacts. Nature Climate Change, 7(6), 403–406. https://doi.org/10.1038/nclimate3301

Fischer, E. M., Sippel, S., & Knutti, R. (2021). Increasing probability of record-shattering climate extremes. Nature Climate Change, 11(8), 689–695. https://doi.org/10.1038/s41558-021-01092-9

Fotso-Nguemo, T. C., Weber, T., Diedhiou, A., Chouto, S., Vondou, D. A., Rechid, D., & Jacob, D. (2023). Projected Impact of Increased Global Warming on Heat Stress and Exposed Population Over Africa. Earth's Future, 11(1), e2022EF003268. https://doi.org/10.1029/2022EF003268

Grant, P. R. (2017). Evolution, climate change, and extreme events. Science, 357(6350), 451–452. https://doi.org/10.1126/science.aao2067

Gu, L., Chen, J., Yin, J., Slater, L. J., Wang, H.-M., Guo, Q., et al. (2022). Global Increases in Compound Flood-Hot Extreme Hazards Under Climate Warming. Geophysical Research Letters, 49(8), e2022GL097726. https://doi.org/10.1029/2022GL097726

Guo, X., Cheng, J., Yin, C., Li, Q., Chen, R., & Fang, J. (2023). The extraordinary Zhengzhou flood of 7/20, 2021: How extreme weather and human response compounding to the disaster. Cities, 134, 104168. https://doi.org/10.1016/j.cities.2022.104168

Islam, N., & Winkel, J. (2017). Climate change and social inequality.

Iturbide, M., Gutiérrez, J. M., Alves, L. M., Bedia, J., Cerezo-Mota, R., Cimadevilla, E., et al. (2020). An update of IPCC climate reference regions for subcontinental analysis of climate model data: definition and aggregated datasets. Earth System Science Data, 12(4), 2959–2970. https://doi.org/10.5194/essd-12-2959-2020

Iyakaremye, V., Zeng, G., Yang, X., Zhang, G., Ullah, I., Gahigi, A., et al. (2021). Increased high-temperature extremes and associated population exposure in Africa by the mid-21st century. Science of The Total Environment, 790, 148162. https://doi.org/10.1016/j.scitotenv.2021.148162

Jones, B., & O'Neill, B. C. (2016). Spatially explicit global population scenarios consistent with the Shared Socioeconomic Pathways. Environmental Research Letters, 11(8), 084003. https://doi.org/10.1088/1748-9326/11/8/084003

Jones, Bryan, O'Neill, B. C., McDaniel, L., McGinnis, S., Mearns, L. O., & Tebaldi, C. (2015). Future population exposure to US heat extremes. Nature Climate Change, 5(7), 652–655. https://doi.org/10.1038/nclimate2631

Klein, T., & Anderegg, W. R. L. (2021). A vast increase in heat exposure in the 21st century is driven by global warming and urban population growth. Sustainable Cities and Society, 73, 103098. https://doi.org/10.1016/j.scs.2021.103098

Kreibich, H., Van Loon, A. F., Schröter, K., Ward, P. J., Mazzoleni, M., Sairam, N., et al. (2022). The challenge of unprecedented floods and droughts in risk management. Nature, 608(7921), 80–86. https://doi.org/10.1038/s41586-022-04917-5

Kumar, R., & Mishra, V. (2020). Increase in Population Exposure Due to Dry and Wet Extremes in India Under a Warming Climate. Earth's Future, 8(12), e2020EF001731. https://doi.org/10.1029/2020EF001731

Levy, A. A. L., Ingram, W., Jenkinson, M., Huntingford, C., Hugo Lambert, F., & Allen, M. (2013). Can correcting feature location in simulated mean climate improve agreement on projected changes? Geophysical Research Letters, 40(2), 354–358. https://doi.org/10.1002/2012GL053964

Lin, N. (2019). Tropical cyclones and heatwaves. Nature Climate Change, 9(8), 579–580. https://doi.org/10.1038/s41558-019-0537-2

Lu, E. (2009). Determining the start, duration, and strength of flood and drought with daily precipitation: Rationale. Geophysical Research Letters, 36(12). https://doi.org/10.1029/2009GL038817

McMichael, A. J. (2015). Extreme weather events and infectious disease outbreaks. Virulence, 6(6), 543–547. https://doi.org/10.4161/21505594.2014.975022

Nangombe, S., Zhou, T., Zhang, W., Wu, B., Hu, S., Zou, L., & Li, D. (2018). Record-breaking climate extremes in Africa under stabilized 1.5 °C and 2 °C global warming scenarios. Nature Climate Change, 8(5), 375–380. https://doi.org/10.1038/s41558-018-0145-6

NWS (National Weather Service). (2011). Heat Index Calculation. Retrieved March 26, 2023, from https://www.wpc.ncep.noaa.gov/html/heatindex.shtml

O'Neill, B. C., Tebaldi, C., van Vuuren, D. P., Eyring, V., Friedlingstein, P., Hurtt, G., et al. (2016). The Scenario Model Intercomparison Project (ScenarioMIP) for CMIP6. Geoscientific Model Development, 9(9), 3461–3482. https://doi.org/10.5194/gmd-9-3461-2016

Park, C.-E., & Jeong, S. (2022). Population Exposure Projections to Intensified Summer Heat. Earth's Future, 10(2), e2021EF002602. https://doi.org/10.1029/2021EF002602

Swain, D. L., Wing, O. E. J., Bates, P. D., Done, J. M., Johnson, K. A., & Cameron, D. R. (2020). Increased Flood Exposure Due to Climate Change and Population Growth in the United States. Earth's Future, 8(11), e2020EF001778. https://doi.org/10.1029/2020EF001778

Thornthwaite, C. W. (1948). An Approach toward a Rational Classification of Climate. Geographical Review, 38(1), 55–94. https://doi.org/10.2307/210739

Thrasher, B., Wang, W., Michaelis, A., Melton, F., Lee, T., & Nemani, R. (2022). NASA Global Daily Downscaled Projections, CMIP6. Scientific Data, 9(1), 262. https://doi.org/10.1038/s41597-022-01393-4

Tuholske, C., Caylor, K., Funk, C., Verdin, A., Sweeney, S., Grace, K., et al. (2021). Global urban population exposure to extreme heat. Proceedings of the National Academy of Sciences, 118(41), e2024792118. https://doi.org/10.1073/pnas.2024792118

Vanos, J. K., Baldwin, J. W., Jay, O., & Ebi, K. L. (2020). Simplicity lacks robustness when projecting heat-health outcomes in a changing climate. Nature Communications, 11(1), 6079. https://doi.org/10.1038/s41467-020-19994-1

Vicente-Serrano, S. M., Beguería, S., & López-Moreno, J. I. (2010). A multiscalar drought index sensitive to global warming: the standardized precipitation evapotranspiration index. Journal of Climate, 23(7), 1696–1718.

Wang, J., Chen, Y., Tett, S. F. B., Yan, Z., Zhai, P., Feng, J., & Xia, J. (2020). Anthropogenically-driven increases in the risks of summertime compound hot extremes. Nature Communications, 11(1), 528. https://doi.org/10.1038/s41467-019-14233-8

Watts, N., Amann, M., Arnell, N., Ayeb-Karlsson, S., Beagley, J., Belesova, K., et al. (2021). The 2020 report of The Lancet Countdown on health and climate change: responding to converging crises. The Lancet, 397(10269), 129–170. https://doi.org/10.1016/S0140-6736(20)32290-X

Weber, T., Bowyer, P., Rechid, D., Pfeifer, S., Raffaele, F., Remedio, A. R., et al. (2020). Analysis of Compound Climate Extremes and Exposed Population in Africa Under Two Different Emission Scenarios. Earth's Future, 8(9), e2019EF001473. https://doi.org/10.1029/2019EF001473

Yin, J., Gentine, P., Slater, L., Gu, L., Pokhrel, Y., Hanasaki, N., et al. (2023). Future socio-ecosystem productivity threatened by compound drought–heatwave events. Nature Sustainability, 1–14. https://doi.org/10.1038/s41893-022-01024-1

Yule, E. L., Hegerl, G., Schurer, A., & Hawkins, E. (2023). Using early extremes to place the 2022 UK heat waves into historical context. Atmospheric Science Letters, e1159.

Zhang, G., Wang, H., Gan, T. Y., Zhang, S., Shi, L., Zhao, J., et al. (2022). Climate Change Determines Future Population Exposure to Summertime Compound Dry and Hot Events. Earth's Future, 10(11), e2022EF003015. https://doi.org/10.1029/2022EF003015

Zhang, Q., She, D., Zhang, L., Wang, G., Chen, J., & Hao, Z. (2022). High Sensitivity of Compound Drought and Heatwave Events to Global Warming in the Future. Earth's Future, 10(11), e2022EF002833. https://doi.org/10.1029/2022EF002833

Zhang, W., & Zhou, T. (2020). Increasing impacts from extreme precipitation on population over China with global warming. Science Bulletin, 65(3), 243–252. https://doi.org/10.1016/j.scib.2019.12.002

Zhao, J.-T., Su, B.-D., mondal, S. K., Wang, Y.-J., Tao, H., & Jiang, T. (2021). Population exposure to precipitation extremes in the Indus River Basin at 1.5 °C, 2.0 °C and 3.0 °C warming levels. Advances in Climate Change Research, 12(2), 199–209. https://doi.org/10.1016/j.accre.2021.03.005

Zscheischler, J., Westra, S., van den Hurk, B. J. J. M., Seneviratne, S. I., Ward, P. J., Pitman, A., et al. (2018). Future climate risk from compound events. Nature Climate Change, 8(6), 469–477. https://doi.org/10.1038/s41558-018-0156-3

[Earth's Future]

Supporting Information for

Future global population exposure to record-breaking climate extremes

Bohao Li[1,2], Kai Liu[1,3,*], Ming Wang[1], Qianzhi Wang[1,4], Qian He[2], Chenxia Li[5]

[1] School of National Safety and Emergency Management, Beijing Normal University, Beijing 100875, China.

[2] Faculty of Geographical Science, Beijing Normal University, Beijing 100875, China.

[3] Collaborative Innovation Centre on Forecast and Evaluation of Meteorological Disasters (CIC-FEMD), Nanjing University of Information Science & Technology, Nanjing 210044, China

[4] School of Systems Science, Beijing Normal University, Beijing 100875, China.

[5] College of Resources, Environment and Tourism, Capital Normal University, Beijing 100048, China

*Corresponding author: Kai Liu (liukai@bnu.edu.cn)

Contents of this file

Introduction

Figures and tables explain some of the information mentioned in the article; all figures and tables are referenced in the main text.

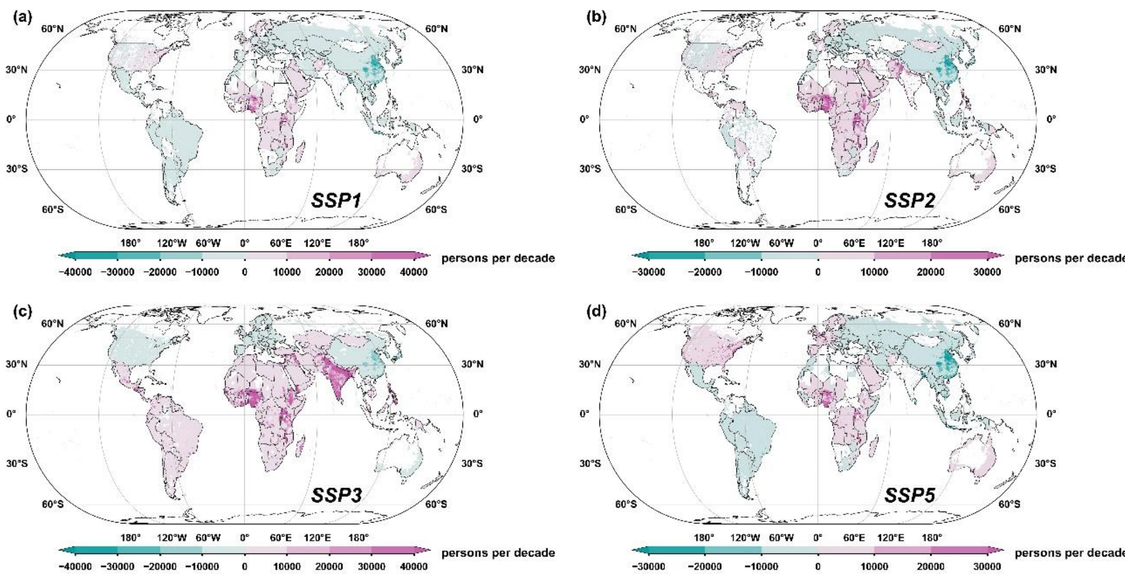

Figure S1. Population trends from 2020 to 2090 based on decadal linear regression at the 0.05 significance level: (a) SSP1, (b) SSP2, (c) SSP3, and (d) SSP5.

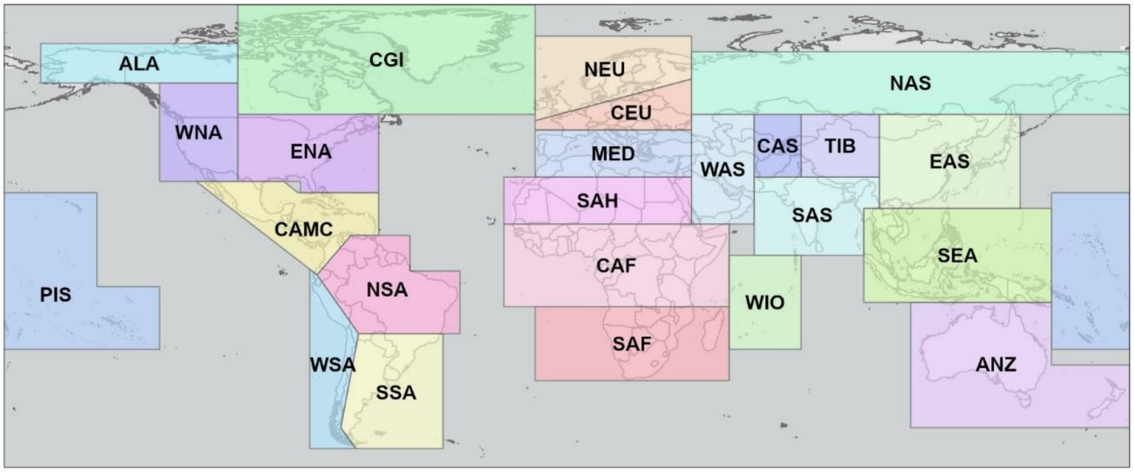

ALA	Alaska/N.W. Canada	ENA	East North America	SAS	South Asia
ANZ	Australia/New Zealand	MED	South Europe/Mediterranean	SEA	Southeast Asia
CAF	Central Africa	NAS	North Asia	SSA	Southeastern South America
CAMC	Central America/Mexico/Caribbean	NEU	North Europe	TIB	Tibetan Plateau
CAS	Central Asia	NSA	Northern South America	WAS	West Asia
CEU	Central Europe	PIS	Pacific Islands	WIO	West Indian Ocean
CGI	Canada/Greenland/Iceland	SAF	Southern Africa	WNA	West North America
EAS	East Asia	SAH	Sahara	WSA	West Coast South America

Figure S2. Climate reference regions used in this study.

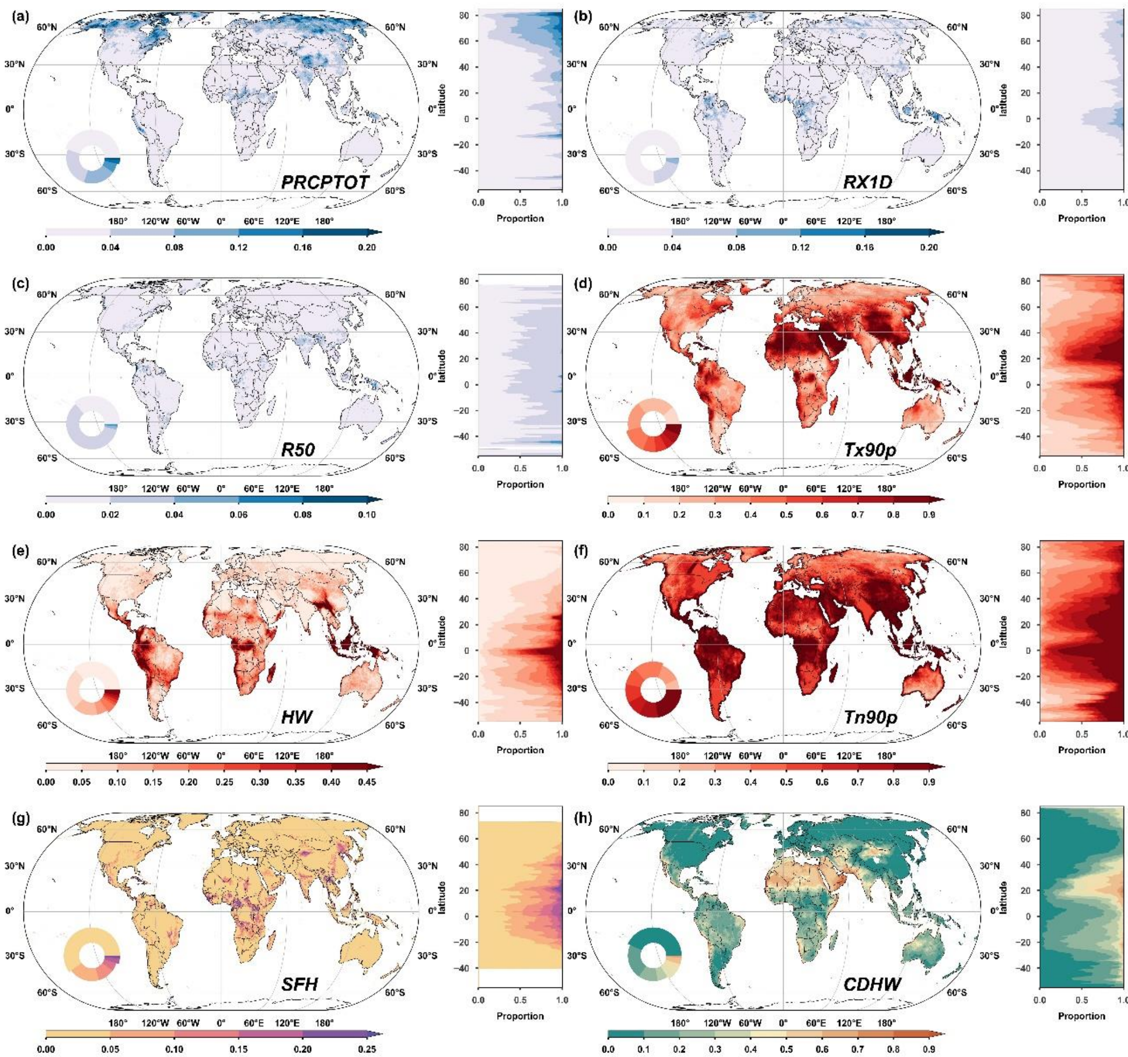

Figure S3. Annual record-breaking probability projections of multimodel medians for different climate extreme indices in the SSP1-2.6 scenario for the late-21st century: (a) PRCPTOT, (b) RX1D, (c) R50, (d) Tx90p, (e) HW, (f) Tn90p, (g) SFH, and (h) CDHW. The rings show the percentages of pixels at different record-breaking probability levels; the stacked charts demonstrate the proportions of record-breaking probability at each level at different latitudes.

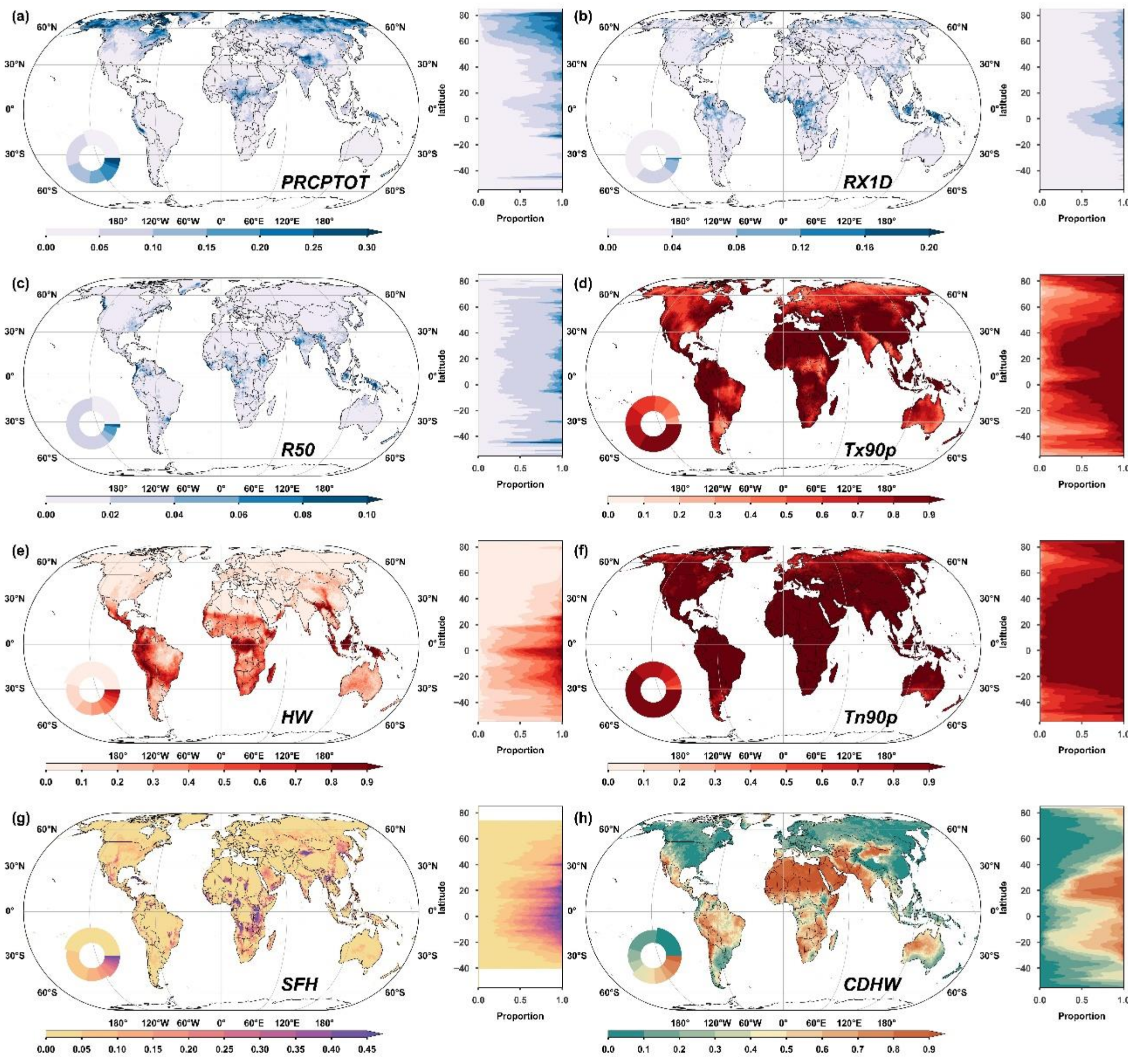

Figure S4. Annual record-breaking probability projections of multimodel medians for different climate extreme indices in the SSP2-4.5 scenario for the late-21st century: (a) PRCPTOT, (b) RX1D, (c) R50, (d) Tx90p, (e) HW, (f) Tn90p, (g) SFH, and (h) CDHW.

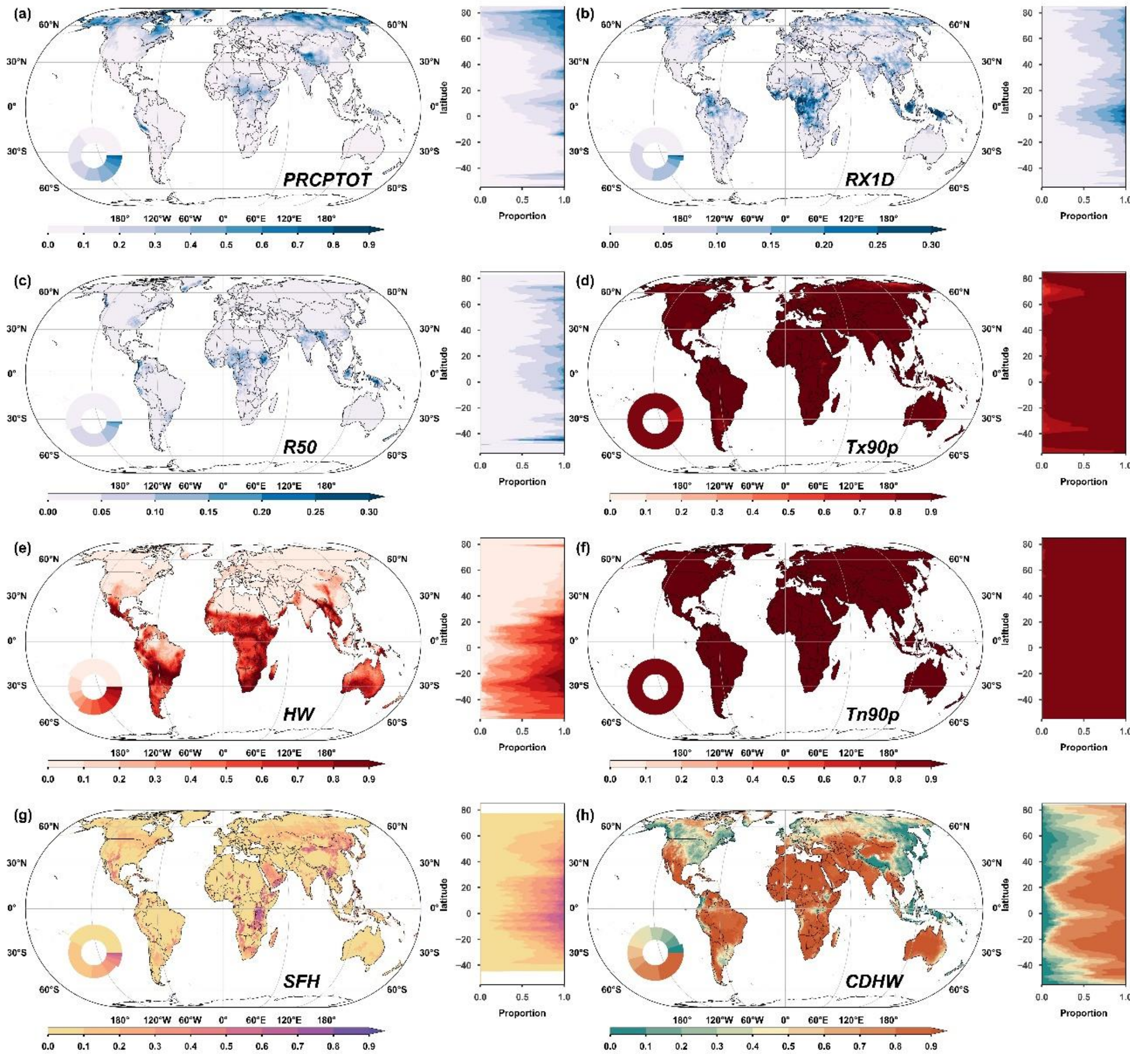

Figure S5. Annual record-breaking probability projections of multimodel medians for different climate extreme indices in the SSP5-8.5 scenario for the late-21st century: (a) PRCPTOT, (b) RX1D, (c) R50, (d) Tx90p, (e) HW, (f) Tn90p, (g) SFH, and (h) CDHW.

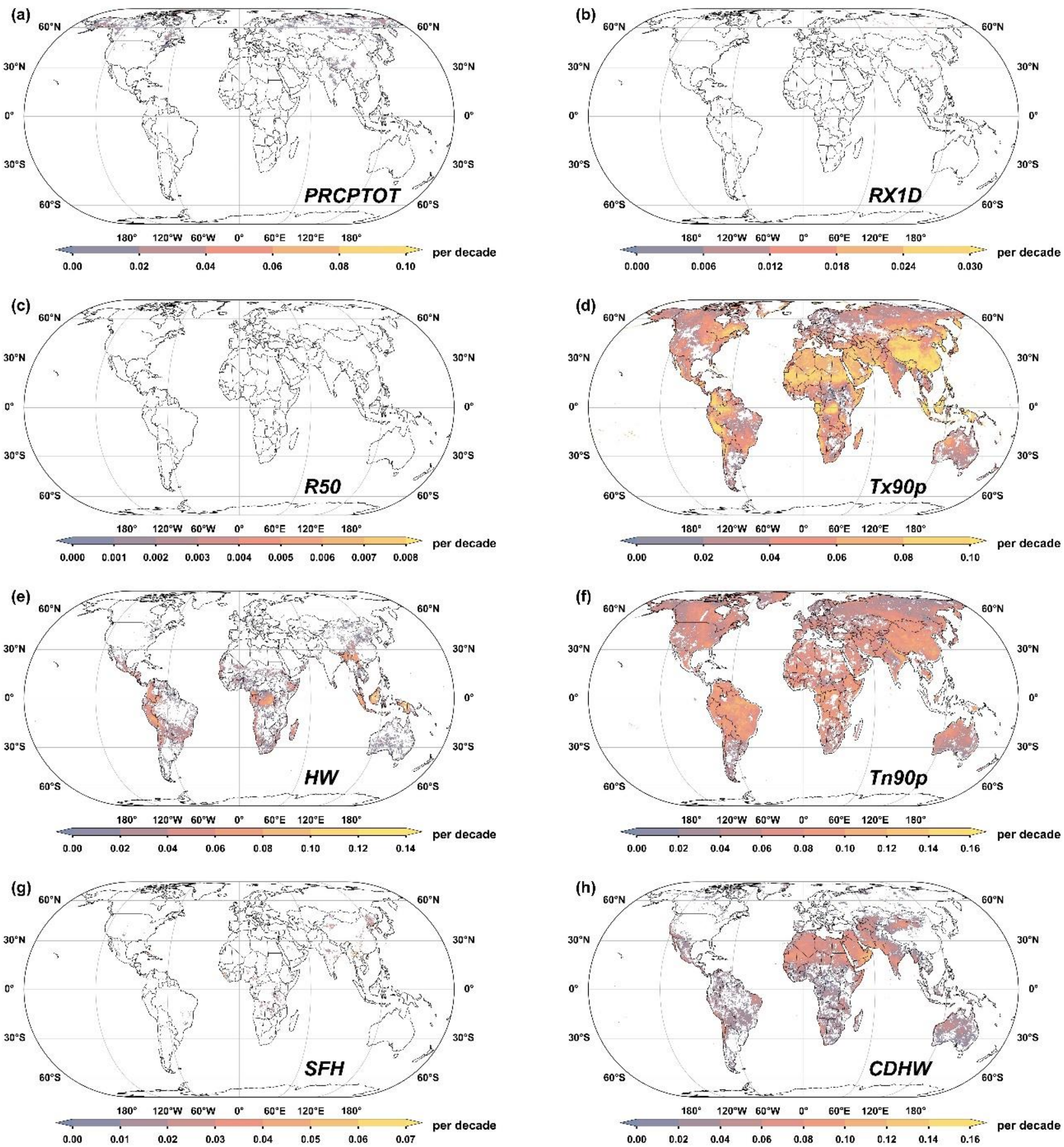

Figure S6. Trends in multimodel median record-breaking probabilities for different indices from the 2020s to 2090s based on decadal linear regression at the 0.05 significance level in the SSP1-2.6 scenario: (a) PRCPTOT, (b) RX1D, (c) R50, (d) Tx90p, (e) HW, (f) Tn90p, (g) SFH, and (h) CDHW.

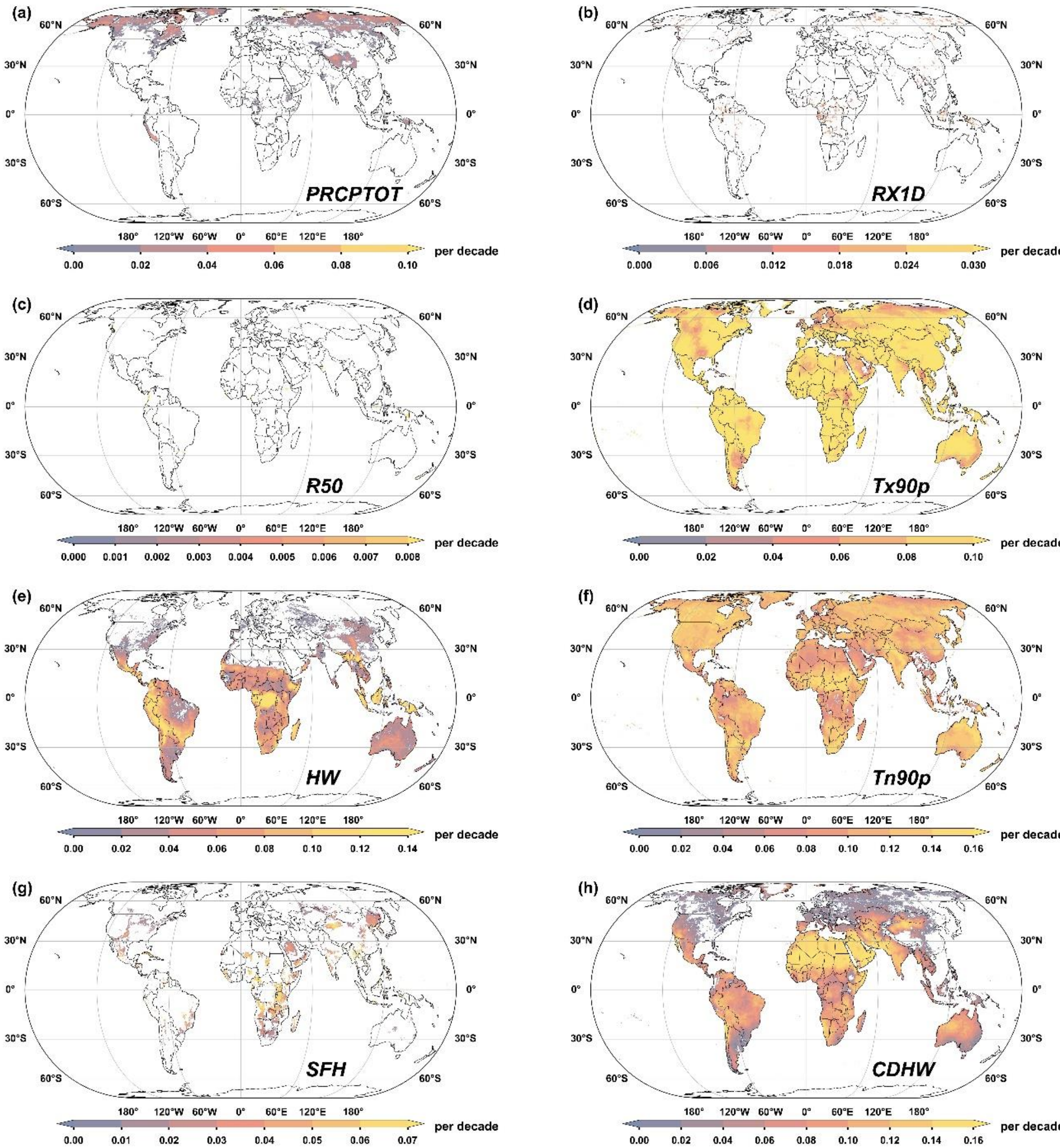

Figure S7. Trends in multimodel median record-breaking probabilities for different indices from the 2020s to 2090s based on decadal linear regression at the 0.05 significance level in the SSP2-4.5 scenario: (a) PRCPTOT, (b) RX1D, (c) R50, (d) Tx90p, (e) HW, (f) Tn90p, (g) SFH, and (h) CDHW.

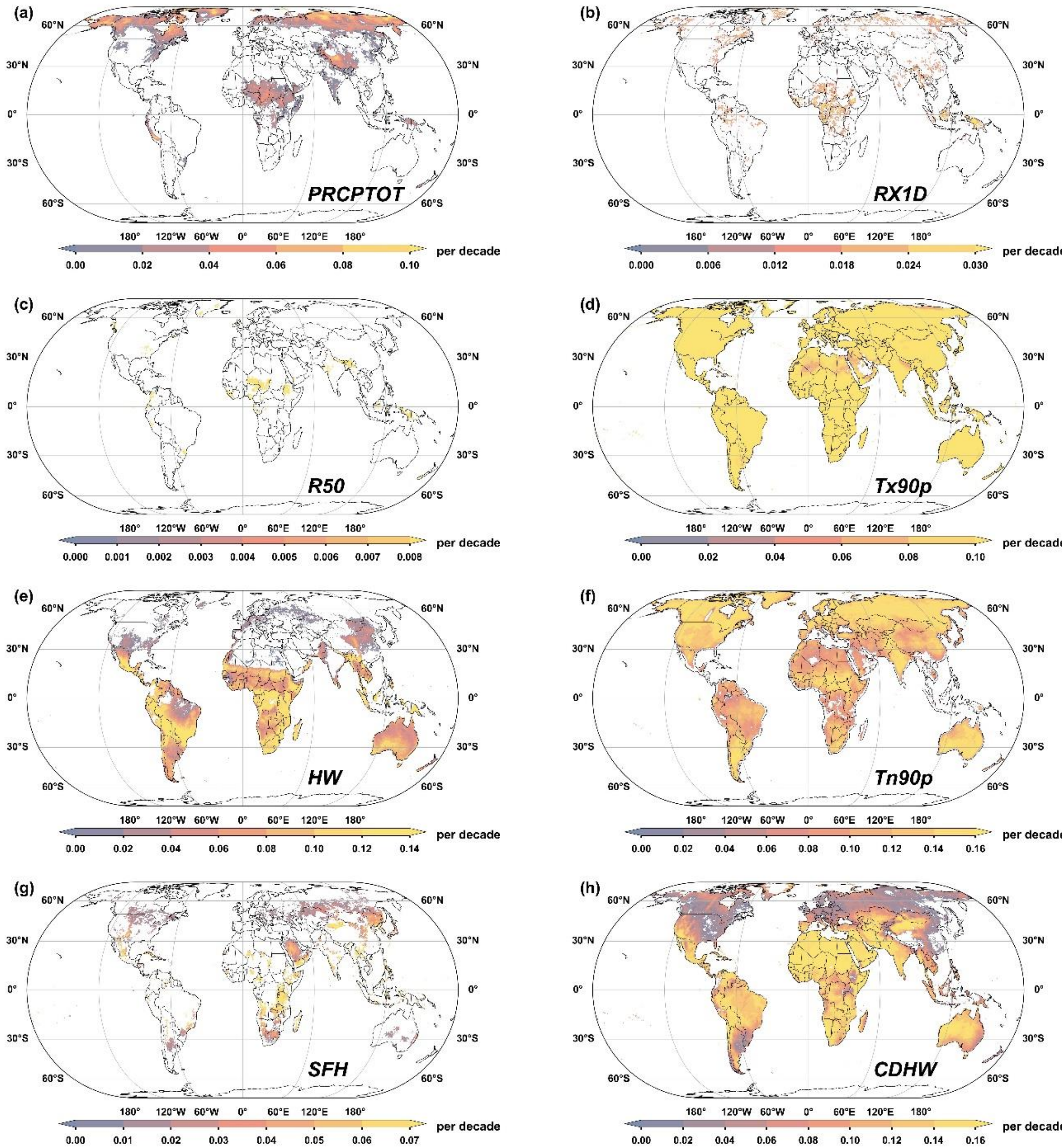

Figure S8. Trends in multimodel median record-breaking probabilities for different indices from the 2020s to 2090s based on decadal linear regression at the 0.05 significance level in the SSP3-7.0 scenario: (a) PRCPTOT, (b) RX1D, (c) R50, (d) Tx90p, (e) HW, (f) Tn90p, (g) SFH, and (h) CDHW.

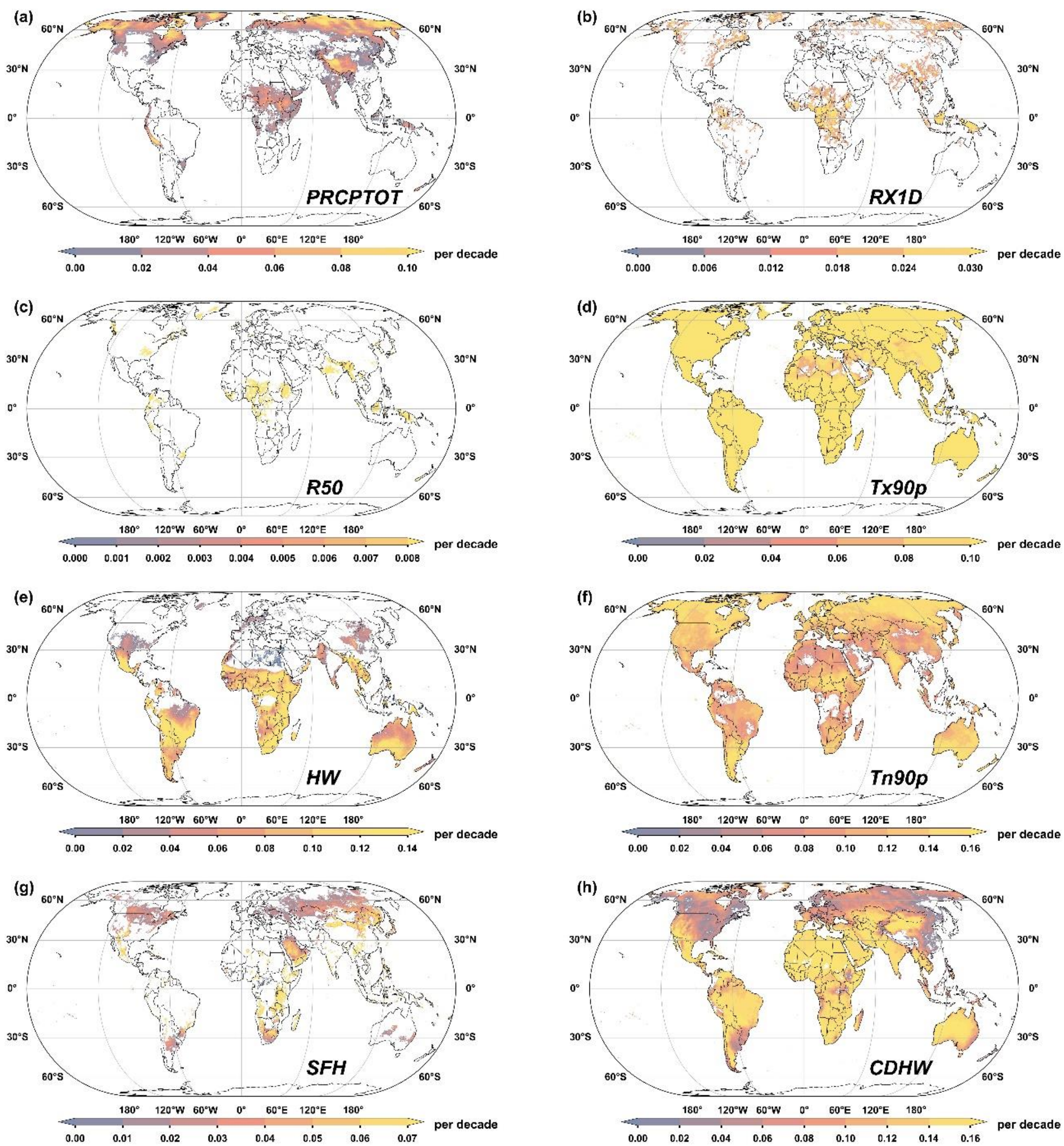

Figure S9. Trends in multimodel median record-breaking probabilities for different indices from the 2020s to 2090s based on decadal linear regression at the 0.05 significance level in the SSP5-8.5 scenario: (a) PRCPTOT, (b) RX1D, (c) R50, (d) Tx90p, (e) HW, (f) Tn90p, (g) SFH, and (h) CDHW.

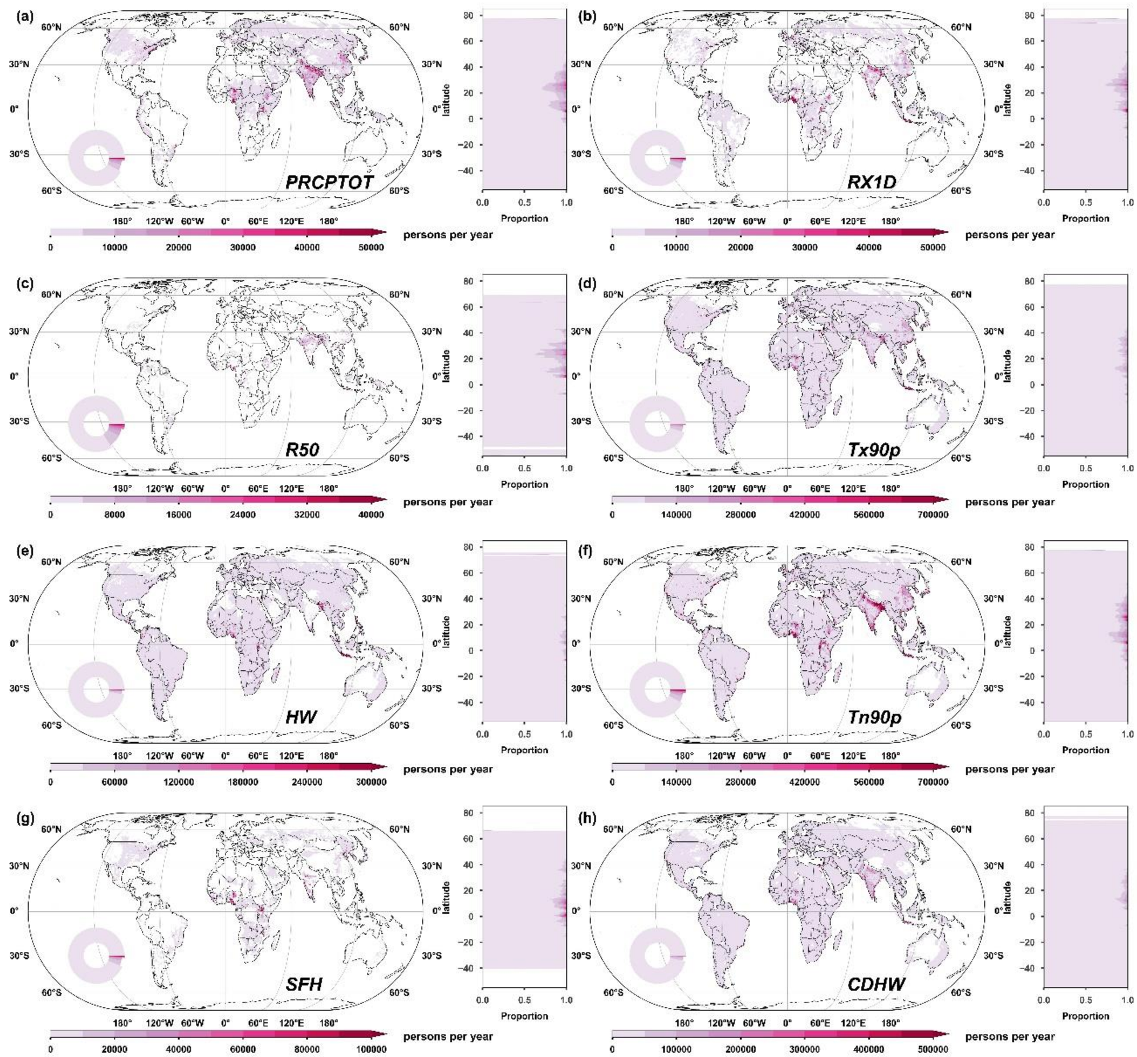

Figure S10. EAE projections of multimodel medians for different climate extreme indices in the SSP1-2.6 scenario for the late-21st century: (a) PRCPTOT, (b) RX1D, (c) R50, (d) Tx90p, (e) HW, (f) Tn90p, (g) SFH, and (h) CDHW. The rings show the percentages of pixels at different population exposure levels; the stacked charts demonstrate the proportions of population exposure at each level at different latitudes.

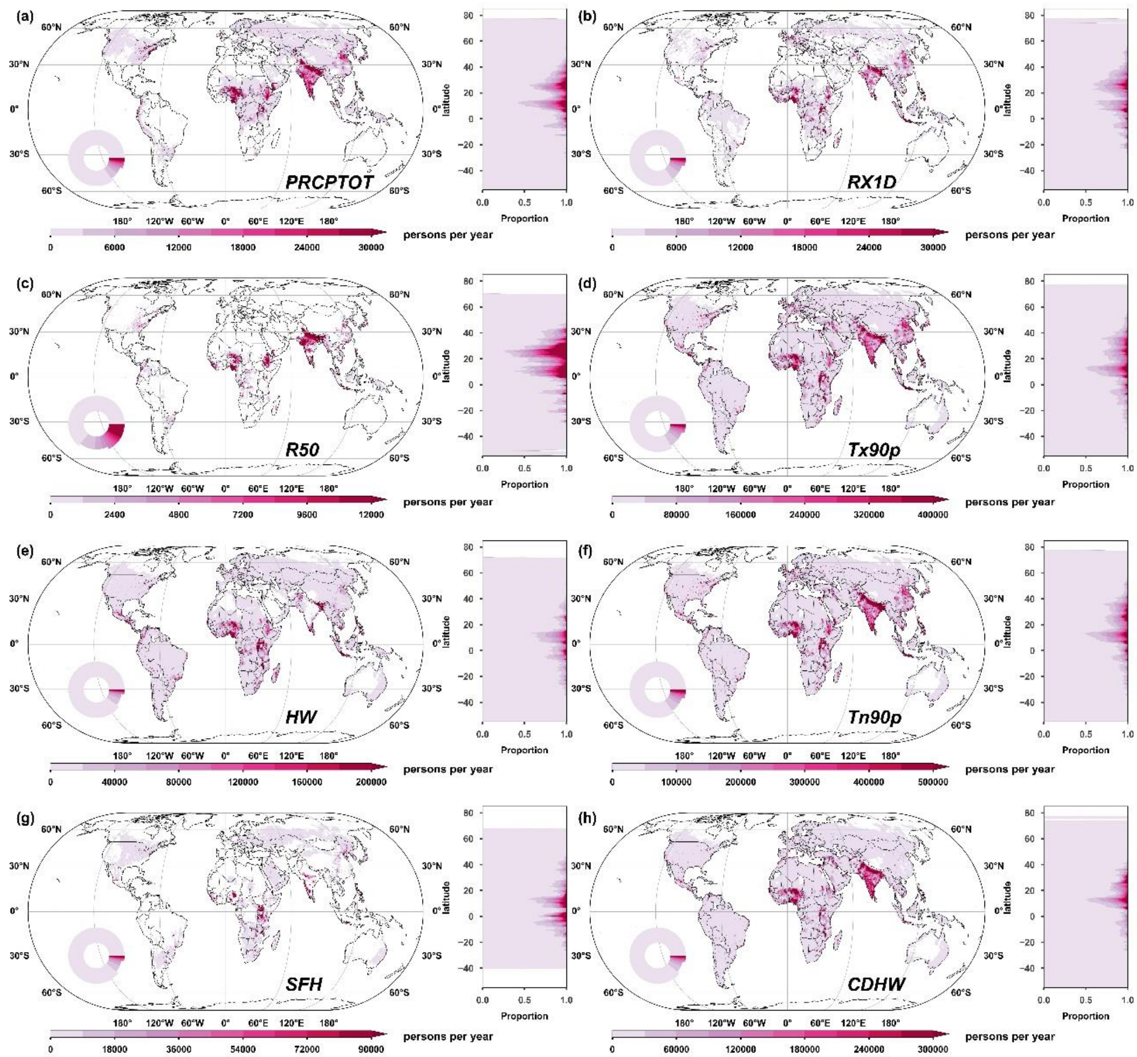

Figure S11. EAE projections of multimodel medians for different climate extreme indices in the SSP2-4.5 scenario for the late-21st century: (a) PRCPTOT, (b) RX1D, (c) R50, (d) Tx90p, (e) HW, (f) Tn90p, (g) SFH, and (h) CDHW.

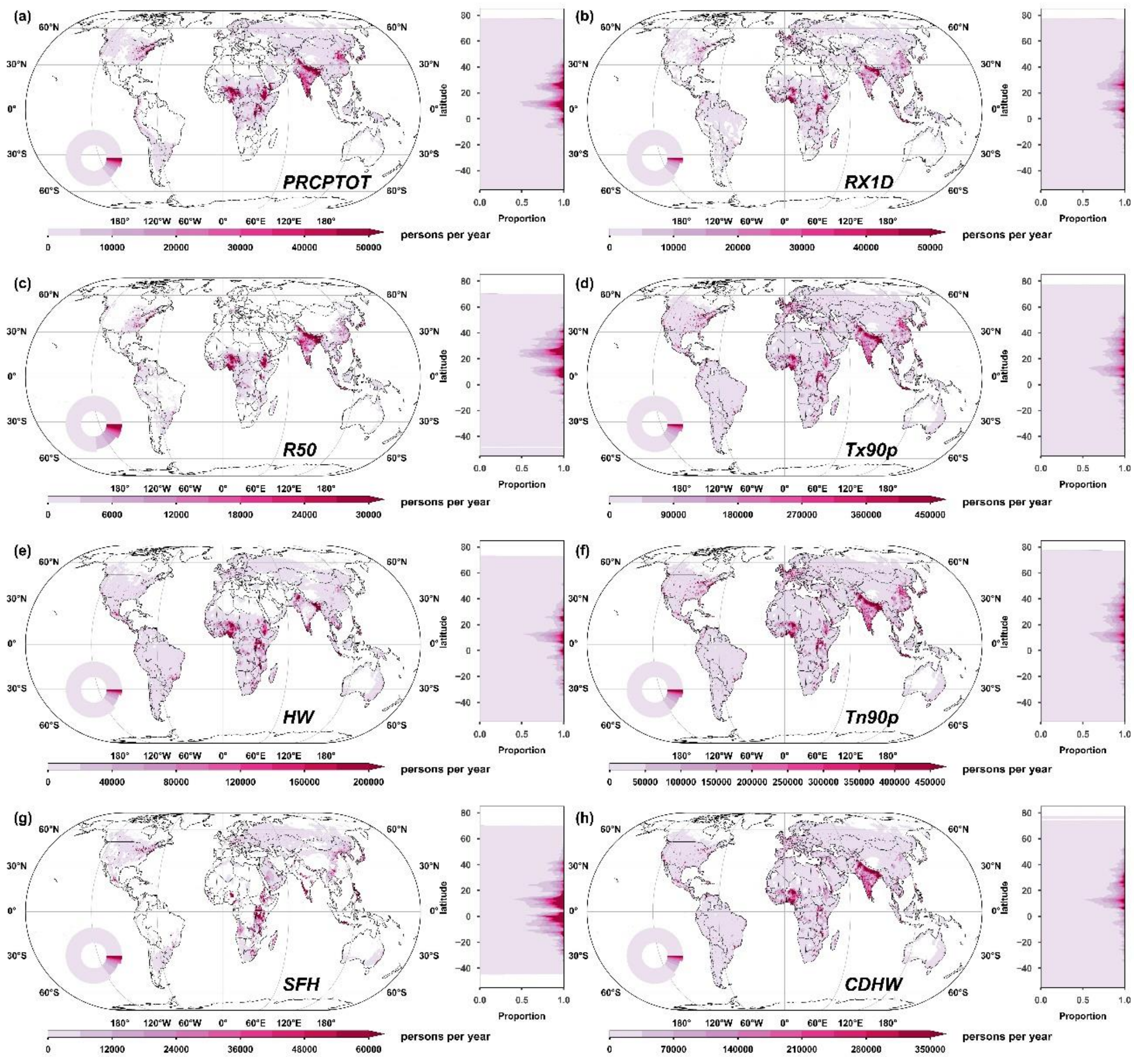

Figure S12. EAE projections of multimodel medians for different climate extreme indices in the SSP5-8.5 scenario for the late-21st century: (a) PRCPTOT, (b) RX1D, (c) R50, (d) Tx90p, (e) HW, (f) Tn90p, (g) SFH, and (h) CDHW.

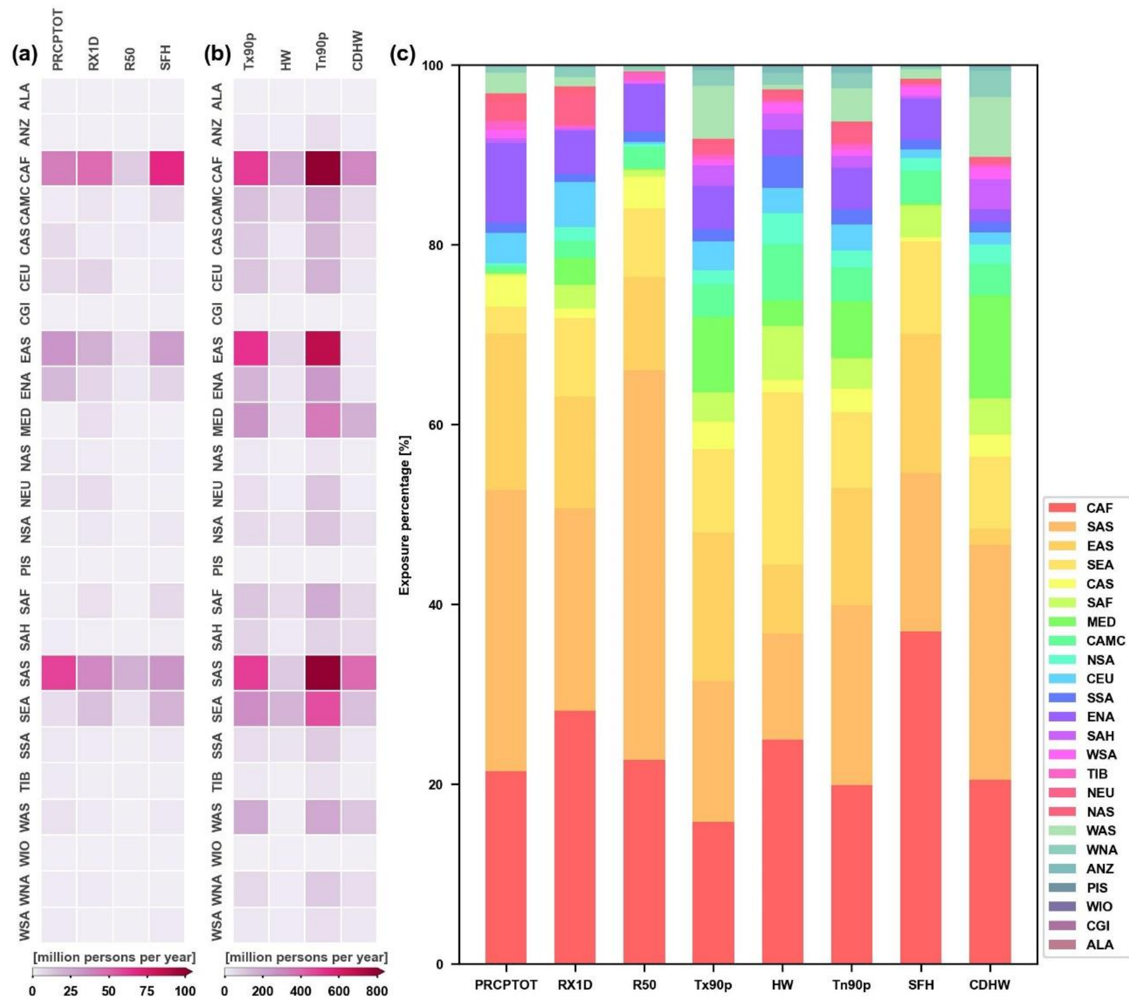

Figure S13. Subcontinental EAE projections of multimodel medians for different climate extreme indices in the SSP1-2.6 scenario for the late-21st century: (a) PRCPTOT, RX1D, R50, and SFH, (b) Tx90p, HW, Tn90p, and CDHW, and (c) regional percentage of the total global EAE.

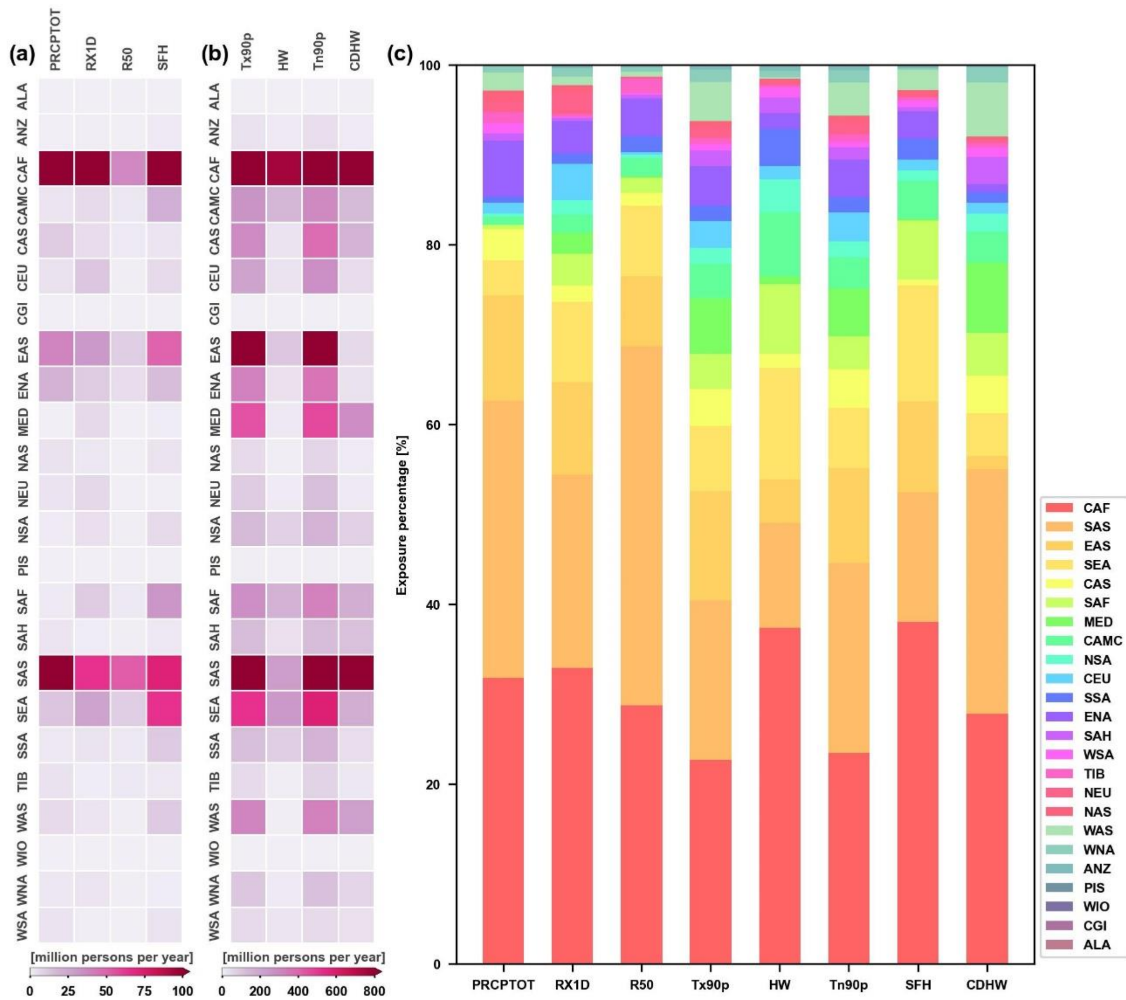

Figure S14. Subcontinental EAE projections of multimodel medians for different climate extreme indices in the SSP2-4.5 scenario for the late-21st century: (a) PRCPTOT, RX1D, R50, and SFH, (b) Tx90p, HW, Tn90p, and CDHW, and (c) regional percentage of the total global EAE.

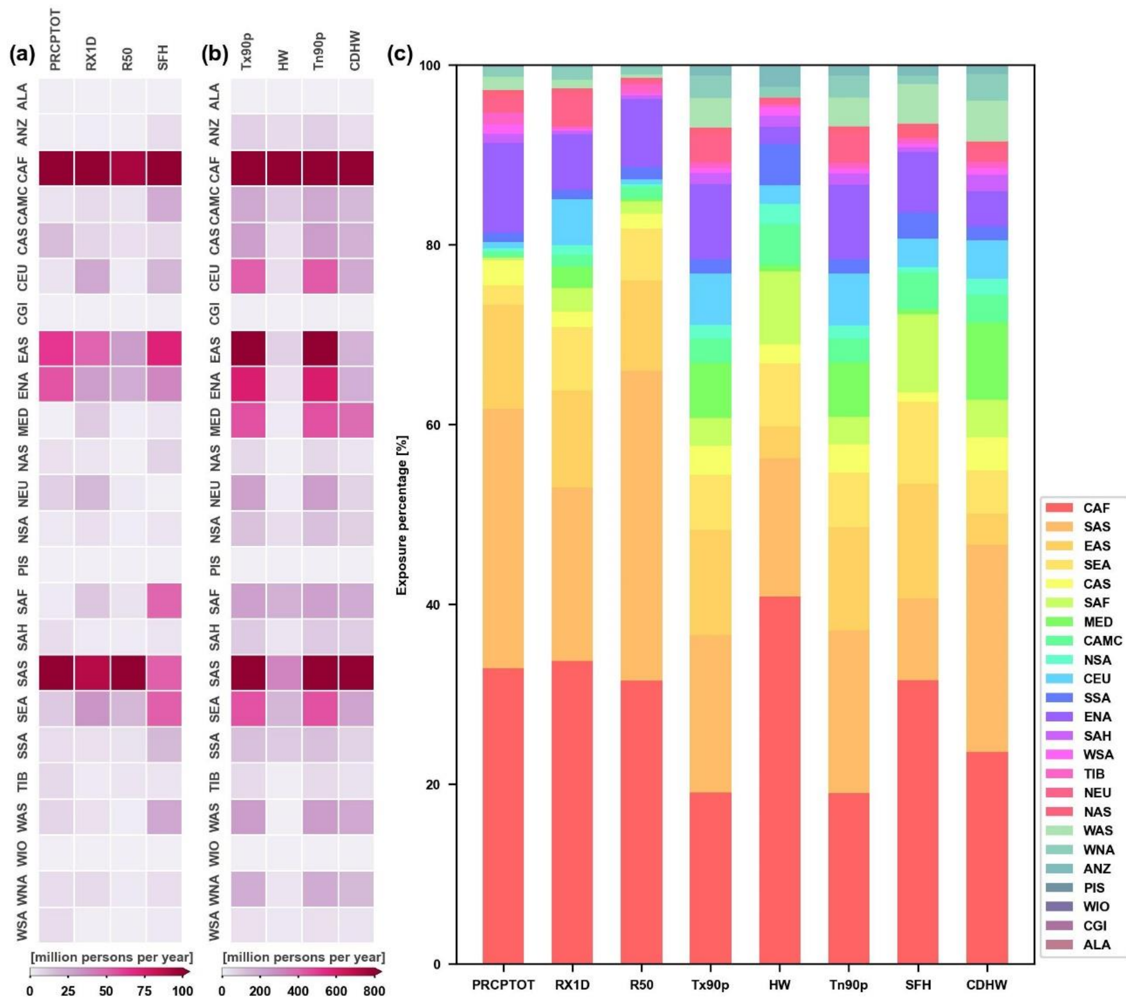

Figure S15. Subcontinental EAE projections of multimodel medians for different climate extreme indices in the SSP5-8.5 scenario for the late-21st century: (a) PRCPTOT, RX1D, R50, and SFH, (b) Tx90p, HW, Tn90p, and CDHW, and (c) regional percentage of the total global EAE.

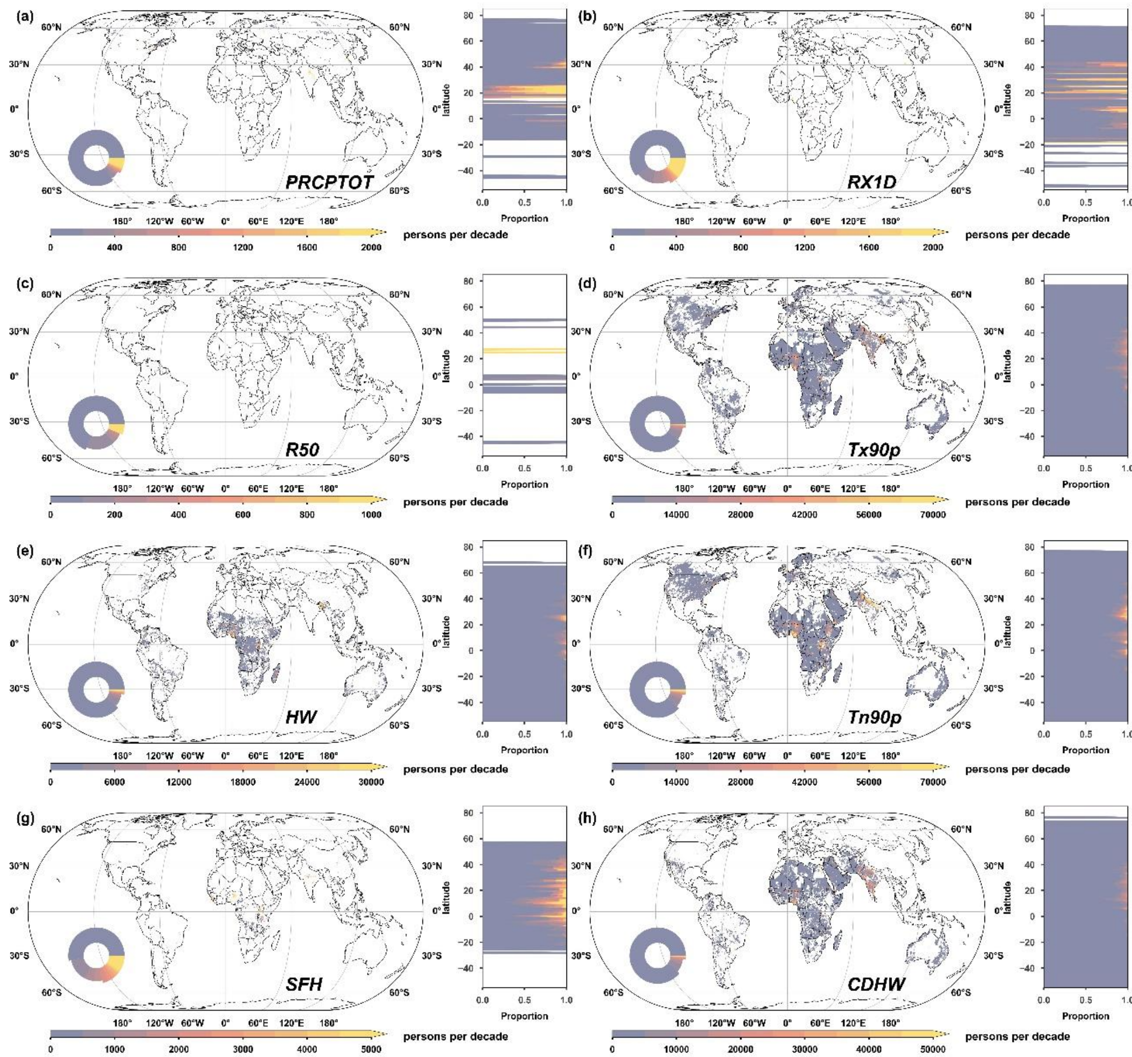

Figure S16. Multimodel median EAE growth rates for different climate extreme indices projected under the SSP1-2.6 scenario from the 2020s to 2090s: (a) PRCPTOT, (b) RX1D, (c) R50, (d) Tx90p, (e) HW, (f) Tn90p, (g) SFH, and (h) CDHW. The rings show the percentage of pixels at different EAE trend levels; the stacked charts demonstrate the percentage of EAE growth rates at each level at different latitudes.

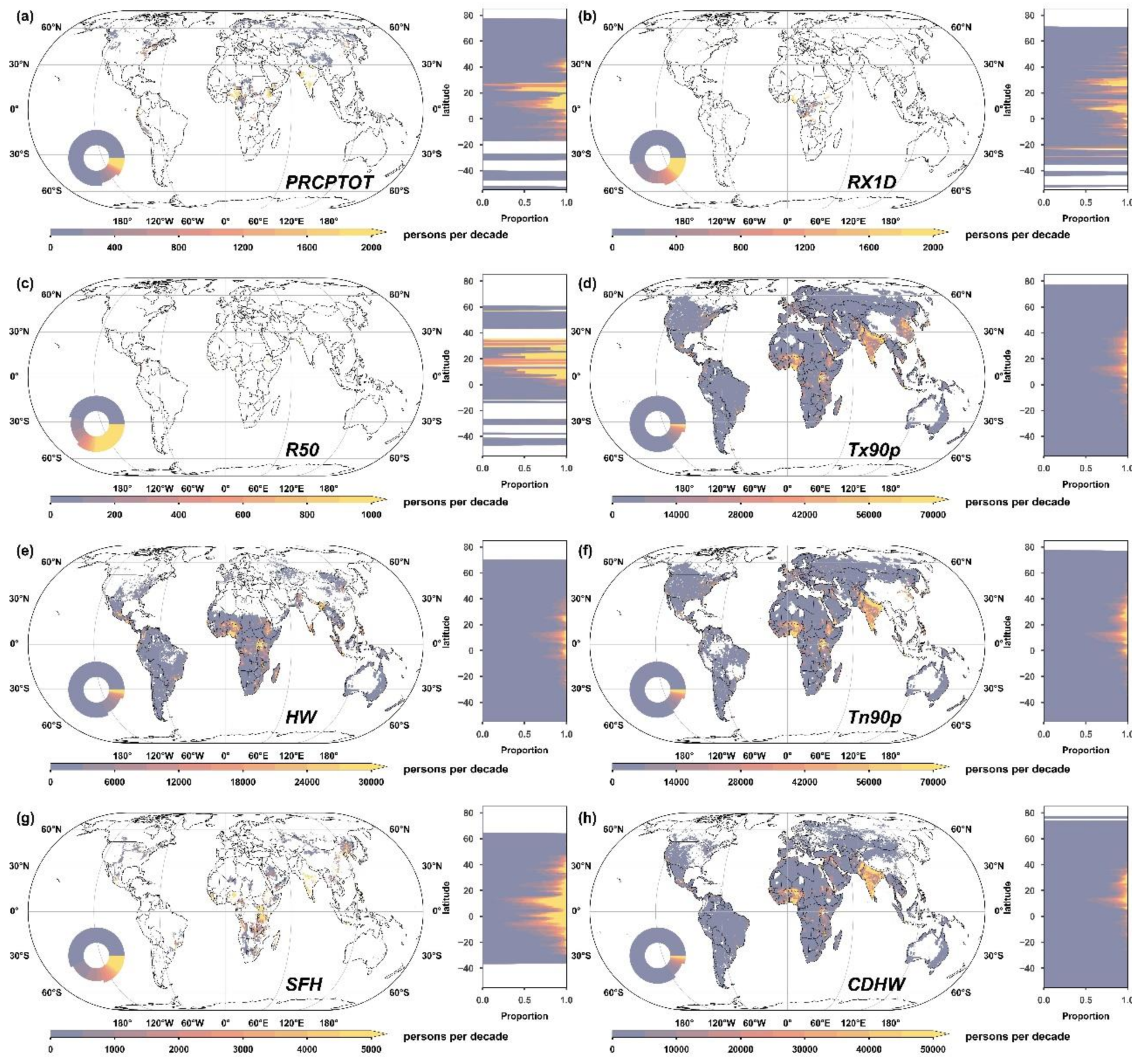

Figure S17. Multimodel median EAE growth rates for different climate extreme indices projected under the SSP2-4.5 scenario from the 2020s to 2090s: (a) PRCPTOT, (b) RX1D, (c) R50, (d) Tx90p, (e) HW, (f) Tn90p, (g) SFH, and (h) CDHW.

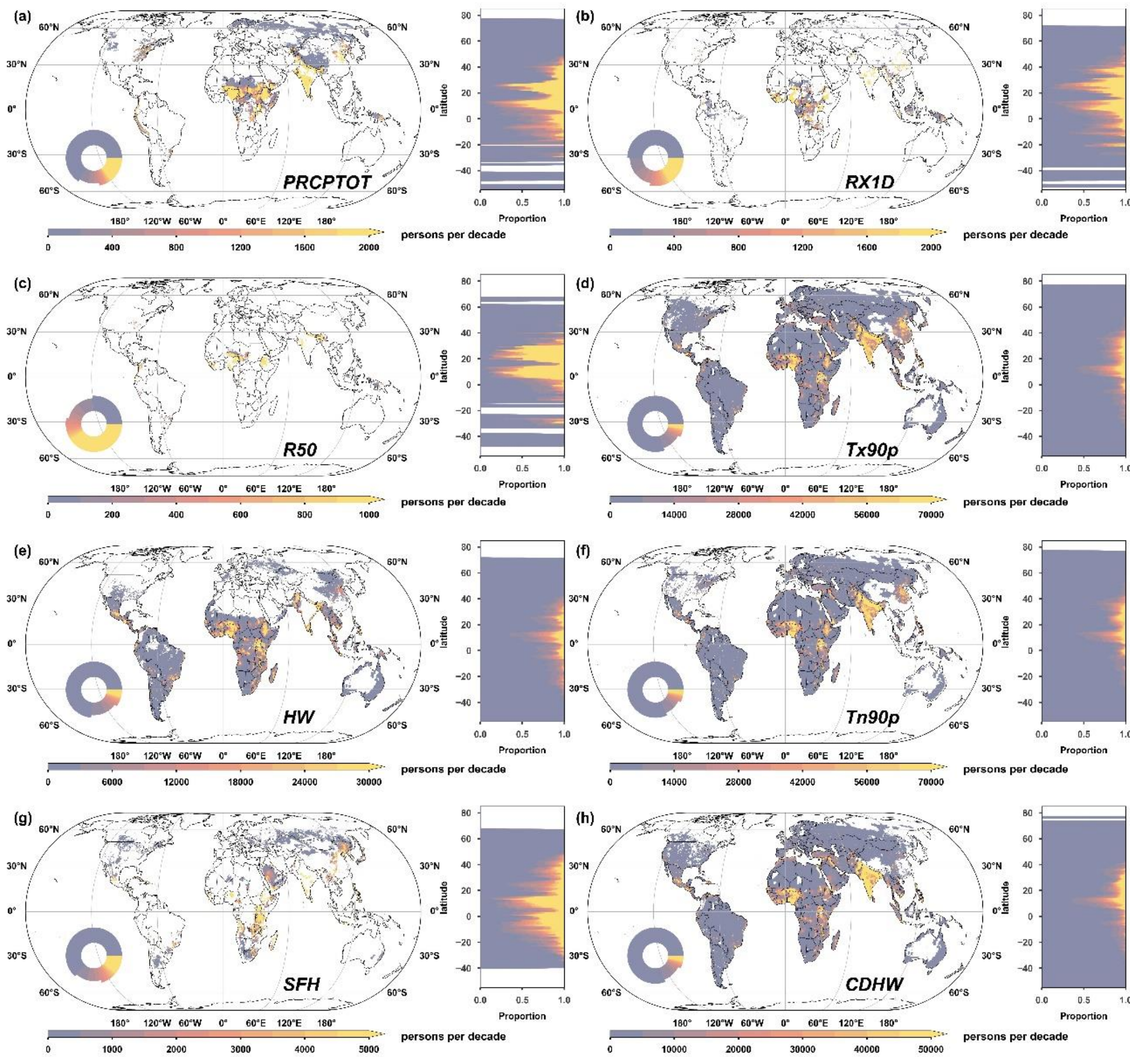

Figure S18. Multimodel median EAE growth rates for different climate extreme indices projected under the SSP3-7.0 scenario from the 2020s to 2090s: (a) PRCPTOT, (b) RX1D, (c) R50, (d) Tx90p, (e) HW, (f) Tn90p, (g) SFH, and (h) CDHW.

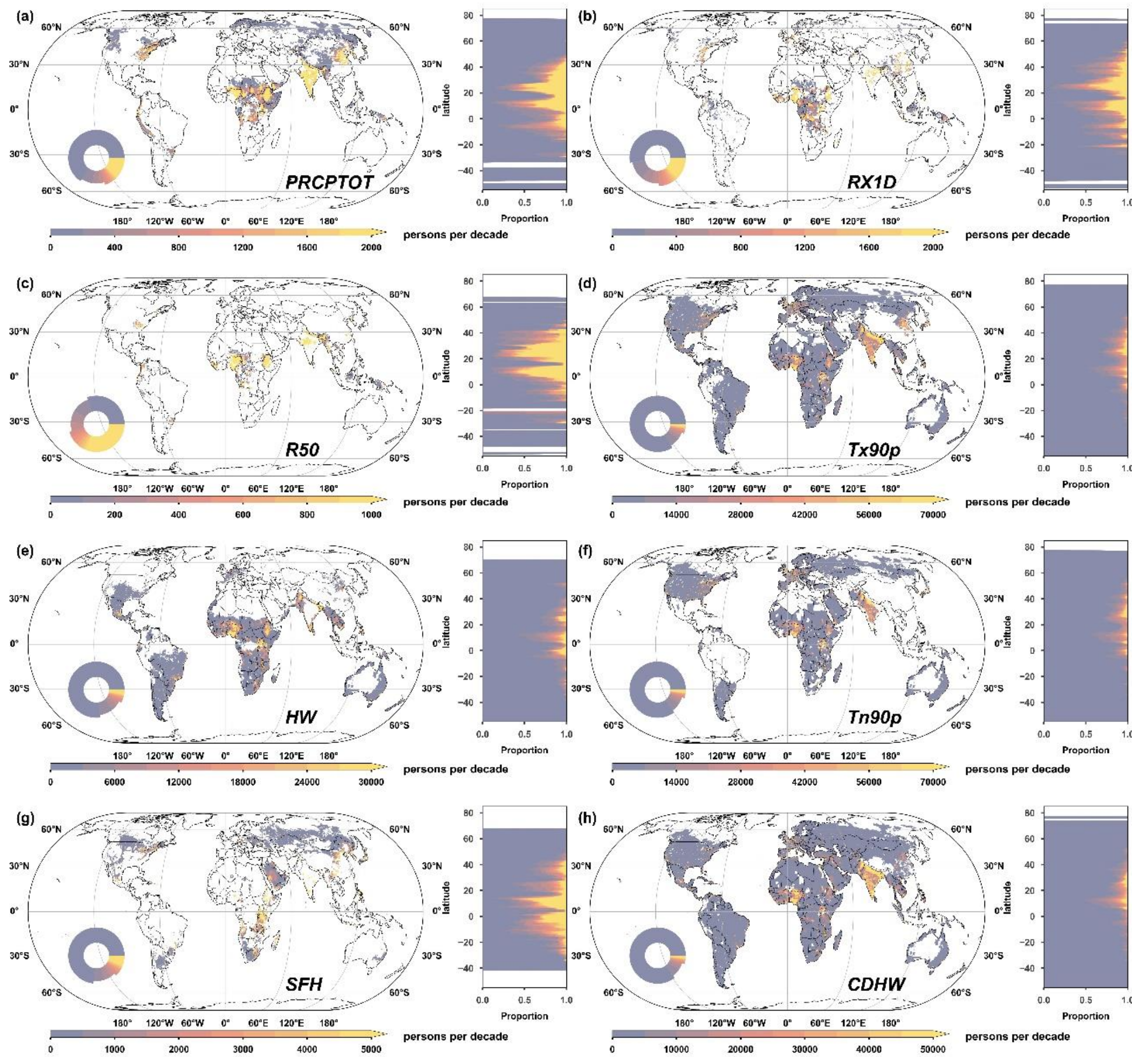

Figure S19. Multimodel median EAE growth rates for different climate extreme indices projected under the SSP5-8.5 scenario from the 2020s to 2090s: (a) PRCPTOT, (b) RX1D, (c) R50, (d) Tx90p, (e) HW, (f) Tn90p, (g) SFH, and (h) CDHW.

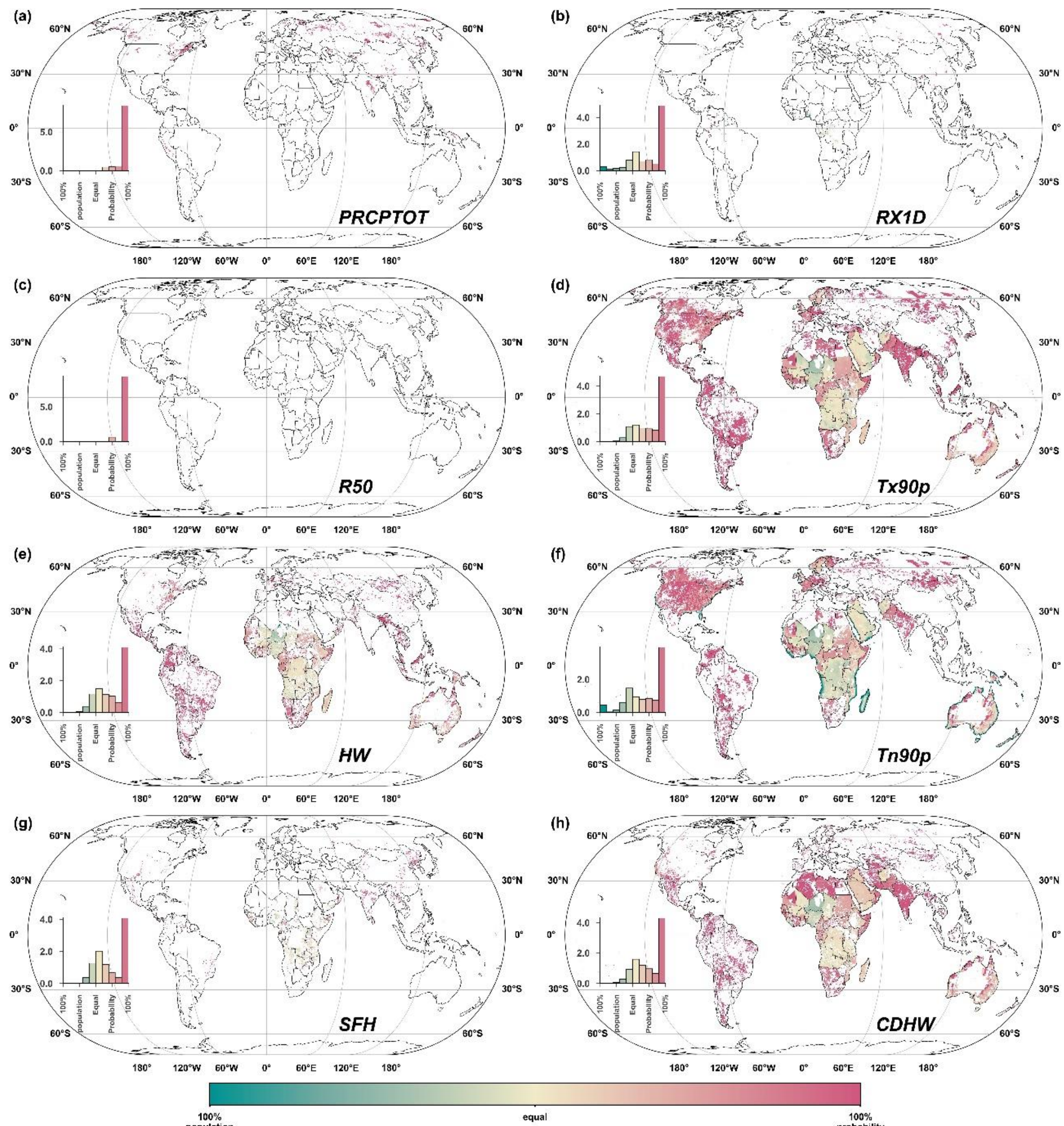

Figure S20. Contributions of record-breaking probability growth and population growth to the multimodel median EAE growth rates for different climate extreme indices projected under the SSP1-2.6 scenario: (a) PRCPTOT, (b) RX1D, (c) R50, (d) Tx90p, (e) HW, (f) Tn90p, (g) SFH, and (h) CDHW. The histograms depict the probability densities at different contribution levels.

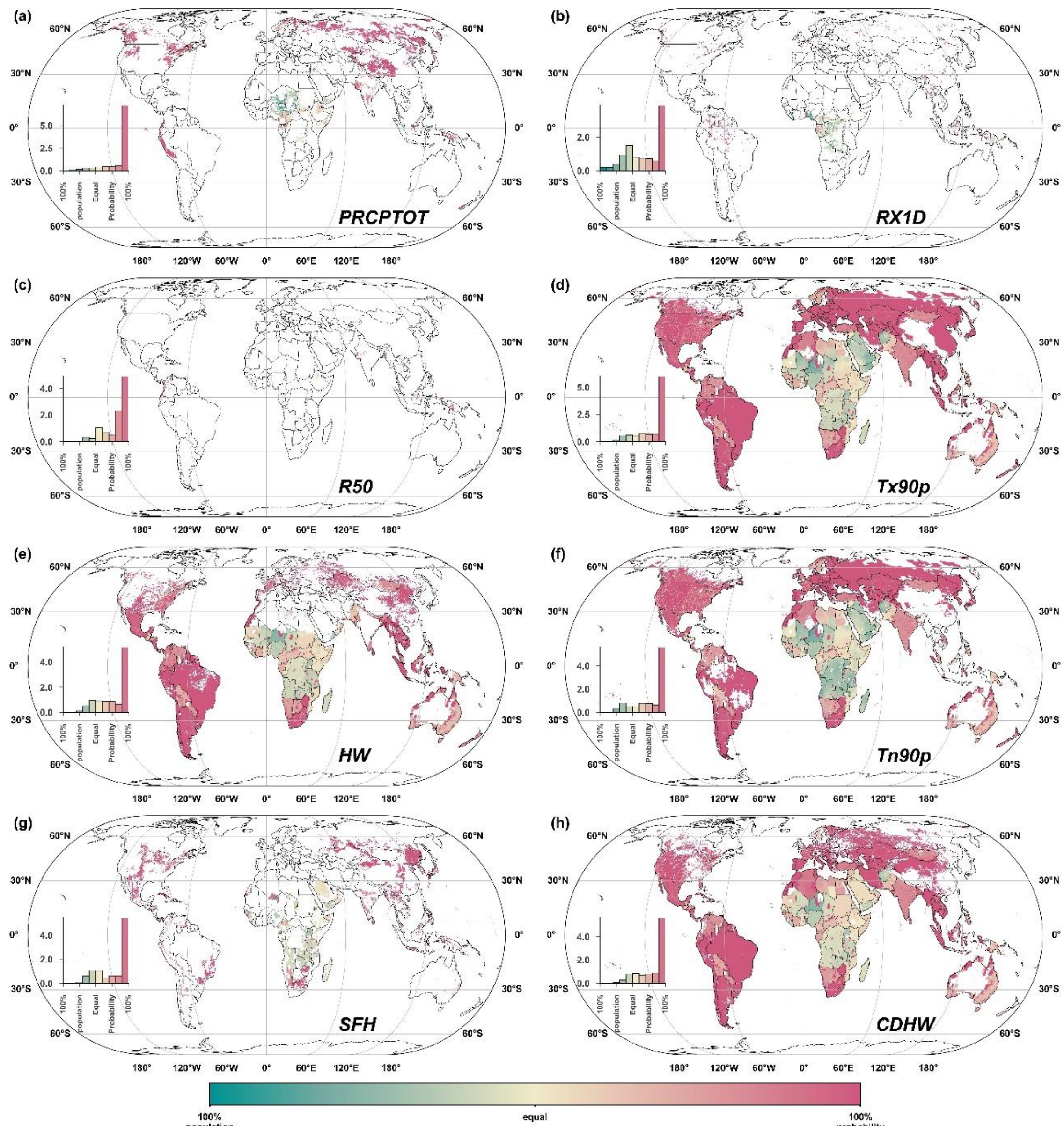

Figure S21. Contributions of record-breaking probability growth and population growth to the multimodel median EAE growth rates for different climate extreme indices projected under the SSP2-4.5 scenario: (a) PRCPTOT, (b) RX1D, (c) R50, (d) Tx90p, (e) HW, (f) Tn90p, (g) SFH, and (h) CDHW. The histograms depict the probability densities at different contribution levels.

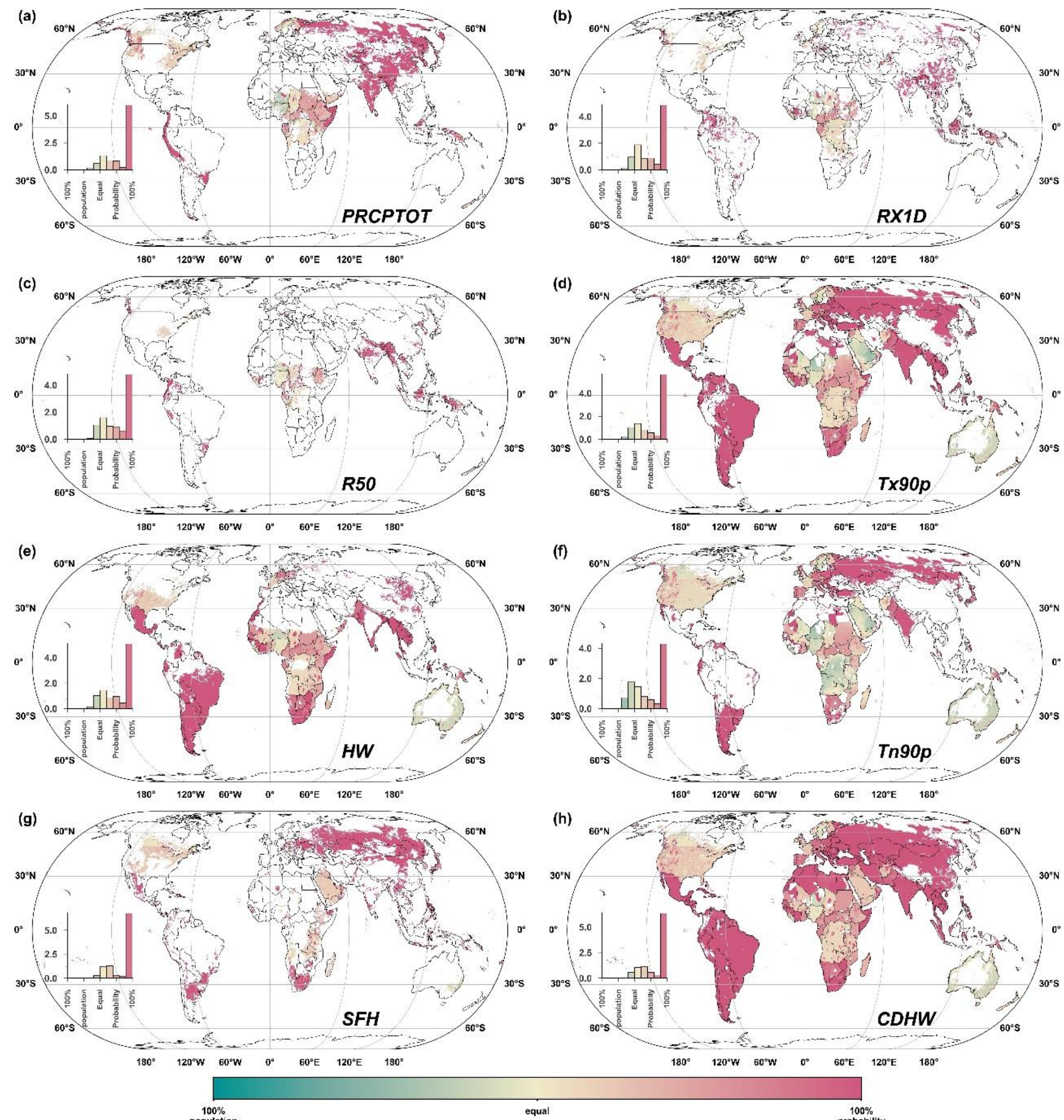

Figure S22. Contributions of record-breaking probability growth and population growth to the multimodel median EAE growth rates for different climate extreme indices projected under the SSP5-8.5 scenario: (a) PRCPTOT, (b) RX1D, (c) R50, (d) Tx90p, (e) HW, (f) Tn90p, (g) SFH, and (h) CDHW. The histograms depict the probability densities at different contribution levels.

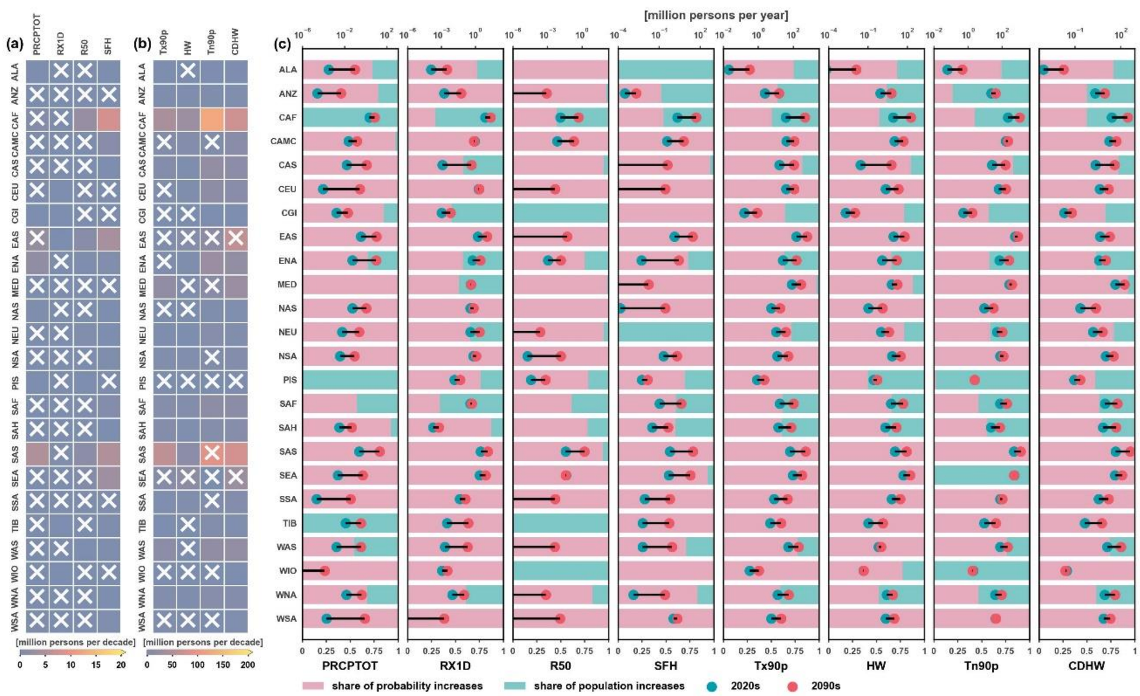

Figure S23. Subcontinental multimodel median EAE variations under the SSP1-2.6 scenario for different climate extreme indices from the 2020s to 2090s: (a) EAE growth rates of PRCPTOT, RX1D, R50, and SFH, (b) EAE growth rates of Tx90p, HW, Tn90p, and CDHW, and (c) Shares of population growth and record-breaking probability growth contributing to the EAE increase in the 2020s and 2090s. The "×" symbols in panels (a) and (b) denote nonsignificant EAE growth (p value <0.05).

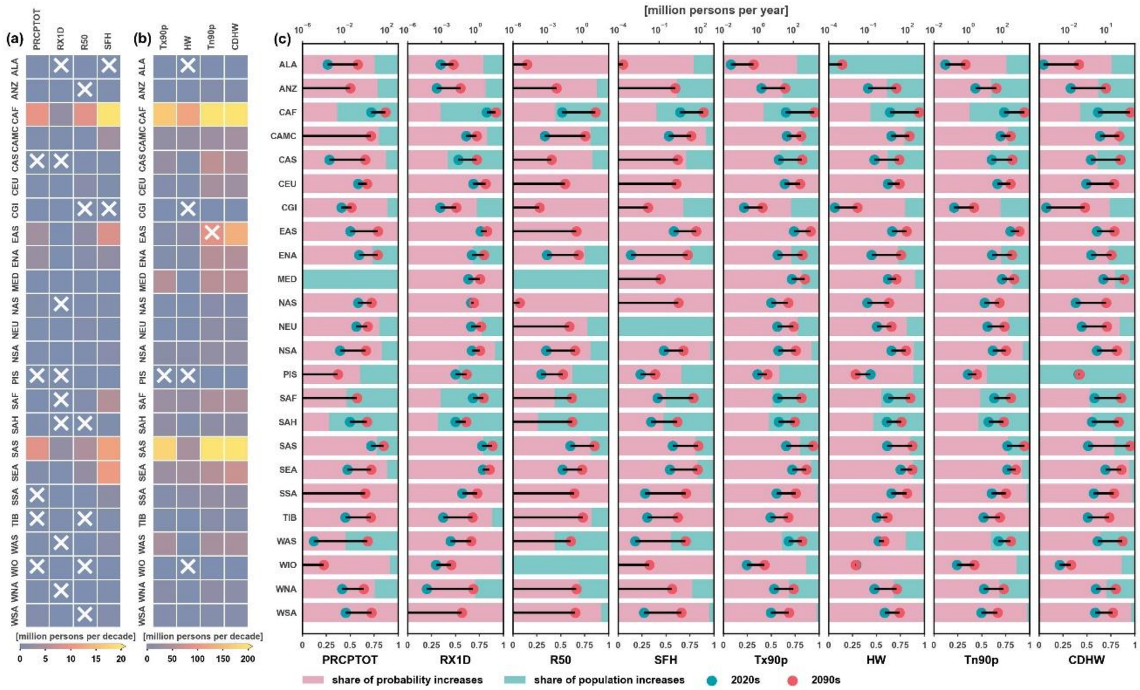

Figure S24. Subcontinental multimodel median EAE variations under the SSP2-4.5 scenario for different climate extreme indices from the 2020s to 2090s: (a) EAE growth rates of PRCPTOT, RX1D, R50, and SFH, (b) EAE growth rates of Tx90p, HW, Tn90p, and CDHW, and (c) shares of population growth and record-breaking probability growth contributing to the EAE increase in the 2020s and 2090s.

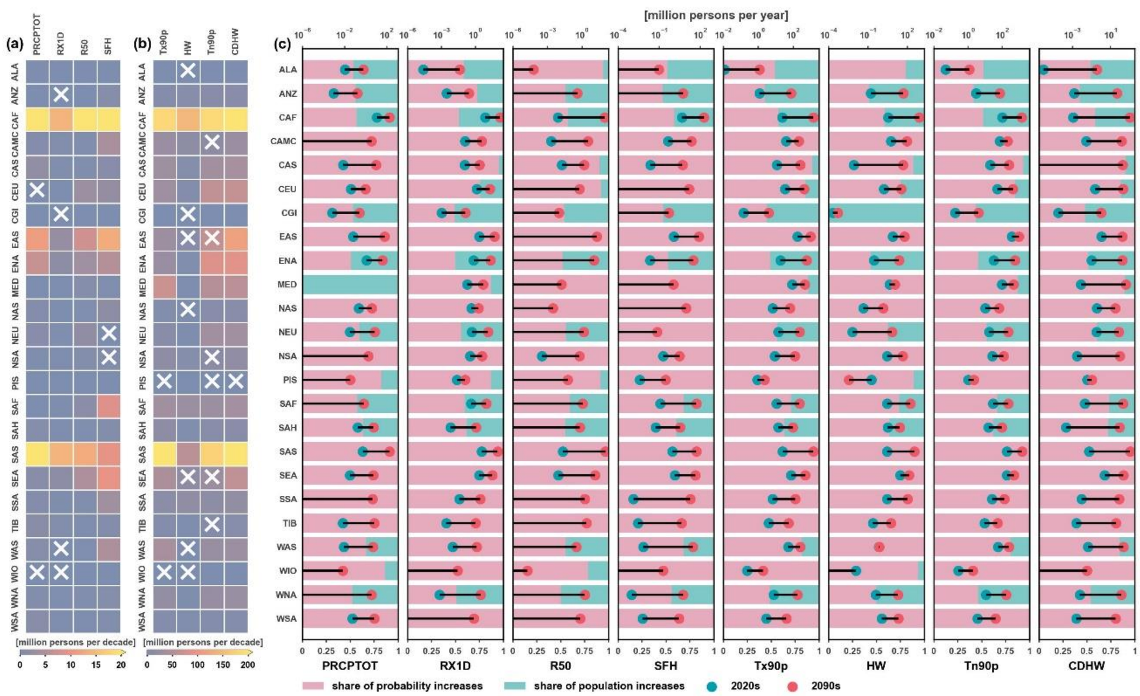

Figure S25. Subcontinental multimodel median EAE variations under the SSP5-8.5 scenario for different climate extreme indices from the 2020s to 2090s: (a) EAE growth rates of PRCPTOT, RX1D, R50, and SFH, (b) EAE growth rates of Tx90p, HW, Tn90p, and CDHW, and (c) shares of population growth and record-breaking probability growth contributing to the EAE increase in the 2020s and 2090s. The “×” symbols in panels (a) and (b) denote nonsignificant EAE growth (p value <0.05).

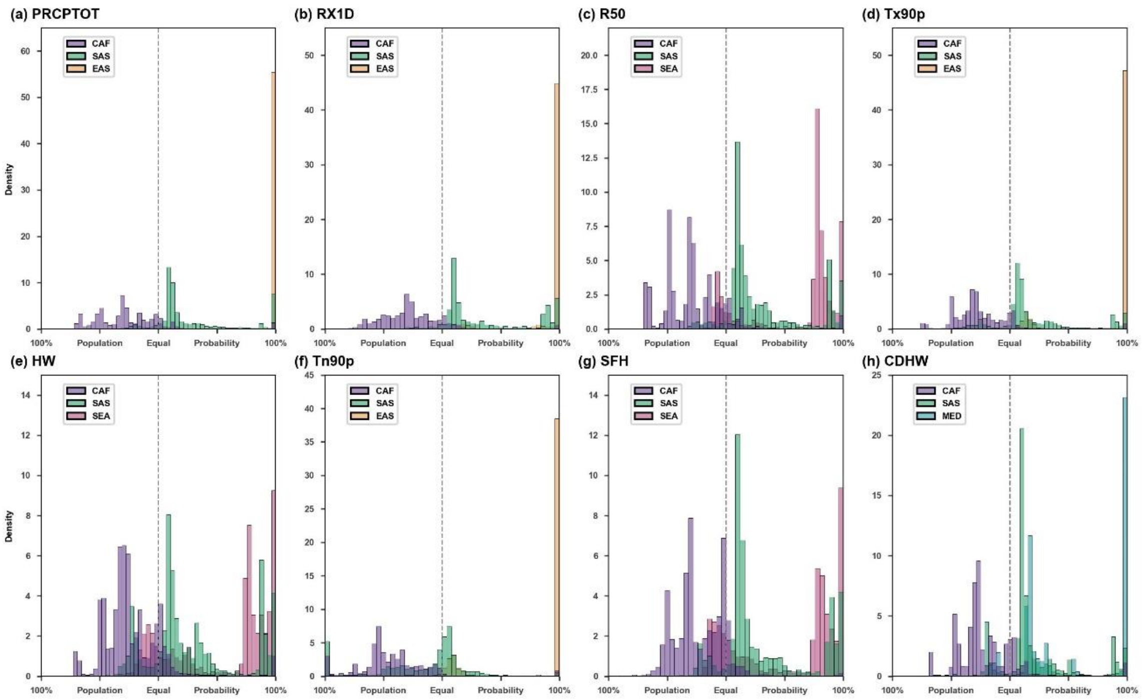

Figure S26. Distributions of the contributions to EAE growth rates in regions with the top three multimodel median EAE growth rates for each climate extreme index under the SSP3-7.0 scenario: (a) PRCPTOT, (b) RX1D, (c) R50, (d) Tx90p, (e) HW, (f) Tn90p, (g) SFH, and (h) CDHW.

Table S1. Summary of the NEX-GDDP-CMIP6 data used in this study. Note: The units of hurs, pr, tas, tasmax, and tasmin are %, kg m-2 s-1, K, K, and K, respectively.

GCM	Institute ID	Variant	Variables	Spatial resolution
ACCESS-CM2	CSIRO-ARCCSS	r1i1p1f1	hurs, pr, tas, tasmax, tasmin	0.25°×0.25°
ACCESS-CM1-5	CSIRO	r1i1p1f1	hurs, pr, tas, tasmax, tasmin	0.25°×0.25°
CanESM5	CCCma	r1i1p1f1	hurs, pr, tas, tasmax, tasmin	0.25°×0.25°
CMCC-ESM2	CMCC	r1i1p1f1	hurs, pr, tas, tasmax, tasmin	0.25°×0.25°
CNRM-CM6-1	CNRM-CERFACS	r1i1p1f2	hurs, pr, tas, tasmax, tasmin	0.25°×0.25°
CNRM-ESM2-1	CNRM-CERFACS	r1i1p1f2	hurs, pr, tas, tasmax, tasmin	0.25°×0.25°
EC-Earth3	EC-Earth-Consortium	r1i1p1f1	hurs, pr, tas, tasmax, tasmin	0.25°×0.25°
EC-Earth3-Veg-LR	EC-Earth-Consortium	r1i1p1f1	hurs, pr, tas, tasmax, tasmin	0.25°×0.25°
GFDL-ESM4	NOAA-GFDL	r1i1p1f1	hurs, pr, tas, tasmax, tasmin	0.25°×0.25°
GISS-E2-1-G	NASA-GISS	r1i1p1f2	hurs, pr, tas, tasmax, tasmin	0.25°×0.25°
INM-CM4-8	INM	r1i1p1f1	hurs, pr, tas, tasmax, tasmin	0.25°×0.25°
INM-CM5-0	INM	r1i1p1f1	hurs, pr, tas, tasmax, tasmin	0.25°×0.25°
IPSL-CM6A-LR	IPSL	r1i1p1f1	hurs, pr, tas, tasmax, tasmin	0.25°×0.25°
KACE-1-0-G	NIMS-KMA	r1i1p1f1	hurs, pr, tas, tasmax, tasmin	0.25°×0.25°
MIROC6	MIROC	r1i1p1f1	hurs, pr, tas, tasmax, tasmin	0.25°×0.25°
MIROC-ES2L	MIROC	r1i1p1f2	hurs, pr, tas, tasmax, tasmin	0.25°×0.25°
MPI-ESM1-2-HR	DKRZ/DWD	r1i1p1f1	hurs, pr, tas, tasmax, tasmin	0.25°×0.25°
MPI-ESM1-2-LR	DKRZ/MPI-M	r1i1p1f1	hurs, pr, tas, tasmax, tasmin	0.25°×0.25°
MRI-ESM2-0	MRI	r1i1p1f1	hurs, pr, tas, tasmax, tasmin	0.25°×0.25°
NorESM2-LM	NCC	r1i1p1f1	hurs, pr, tas, tasmax, tasmin	0.25°×0.25°
NorESM2-MM	NCC	r1i1p1f1	hurs, pr, tas, tasmax, tasmin	0.25°×0.25°
UKESM1-0-LL	MOHC/NIMS-KMA	r1i1p1f2	hurs, pr, tas, tasmax, tasmin	0.25°×0.25°

Table S2. Global EAE differences among scenarios in the late-21st century.

	SSP1-2.6	SSP2-4.5	SSP3-7.0	SSP5-8.5	SSP3-7.0/SSP1-2.6	SSP3-7.0/SSP2-4.5	SSP3-7.0/SSP5-8.5
PRCPTOT	192258875	3.29E+08	7.65E+08	5.47E+08	3.980597	2.324469	1.398486
RX1D	168492367	3.03E+08	6.45E+08	4.66E+08	3.82751	2.12987	1.382641
R50	48090887	1.31E+08	4E+08	2.99E+08	8.327843	3.049114	1.340421
Tx90p	3.123E+09	7.16E+09	1.14E+10	7.23E+09	3.649899	1.591176	1.577254
HW	812676688	2.03E+09	4E+09	2.03E+09	4.920138	1.969438	1.971175
Tn90p	5.363E+09	8.72E+09	1.26E+10	7.37E+09	2.353592	1.446928	1.713328
SFH	187447441	5.02E+08	1.02E+09	5.69E+08	5.438645	2.032117	1.793208
CDHW	1.469E+09	3.72E+09	7.75E+09	4.4E+09	5.27489	2.081912	1.761066

Note: Columns with yellow headings represent the total global EAE (unit: persons per year), and columns with blue headings refer to the ratio of the total global EAE under different scenarios.

Table S3. Global EAE trend differences among scenarios from the 2020s to the 2090s.

	SSP1-2.6	SSP2-4.5	SSP3-7.0	SSP5-8.5	SSP3-7.0/SSP1-2.6	SSP3-7.0/SSP2-4.5	SSP3-7.0/SSP5-8.5
PRCPTOT	10155308	28061378	96678909	80204577	9.520037	3.445266	1.205404
RX1D	6590453	21626790	65972050	59677203	10.01025	3.050478	1.105482
R50	580158.7	5144814	34799273	36185485	59.98233	6.763952	0.961691
Tx90p	3.91E+08	1.08E+09	1.65E+09	1.13E+09	4.216491	1.526406	1.46027
HW	98313704	3.09E+08	5.71E+08	3.35E+08	5.804647	1.84499	1.702428
Tn90p	3.86E+08	1.12E+09	1.36E+09	8.82E+08	3.515161	1.212485	1.538487
SFH	22120686	74174628	1.47E+08	93736479	6.631342	1.977628	1.564917
CDHW	1.88E+08	6.14E+08	1.19E+09	8.15E+08	6.328319	1.936713	1.458646

Note: Columns with yellow headings represent the total global EAE growth rates (unit: persons per decade), and columns with blue headings refer to the ratio of the total global EAE growth rates under different scenarios.

Table S4. Differences in the contribution of record-breaking probability growth driving global EAE growth under different scenarios.

	SSP1-2.6	SSP2-4.5	SSP3-7.0	SSP5-8.5	SSP1-2.6/SSP3-7.0	SSP2-4.5/SSP3-7.0	SSP5-8.5/SSP3-7.0
PRCPTOT	0.53112047	0.73453693	1.04011763	0.91603067	1.95834597	1.38299495	1.72471355
RX1D	0.55770639	0.70651638	0.93554593	0.88338629	1.67748827	1.26682497	1.58396301
R50	0.48745277	0.67417356	0.90406021	0.86903811	1.85466217	1.38305412	1.782815
Tx90p	0.62300207	0.80489629	1.0640211	0.93371123	1.70789336	1.29196407	1.49872894
HW	0.50641718	0.70048422	0.9782655	0.84715112	1.93173837	1.38321575	1.67283251
Tn90p	0.50888373	0.76829548	1.05459589	0.93190456	2.07237101	1.50976625	1.83127207
SFH	0.55768418	0.73357879	0.96654284	0.93720827	1.73313656	1.31540183	1.68053587
CDHW	0.54101108	0.68817723	0.86211048	0.88159943	1.59351723	1.27202058	1.62954043

Note: Columns with yellow headings represent the contribution of record-breaking probability growth driving global EAE growth, and columns with blue headings refer to the ratio of contributions under different scenarios